Modulating Electric Field Distribution by Alkali Cations for CO_2 Electroreduction in Strongly Acidic Medium

Authors: Jun Gu [1,2], Shuo Liu [3], Weiyan Ni [1], Wenhao Ren [1], Sophia Haussener [3] and Xile Hu [1]*

Affiliation:

1. Laboratory of Inorganic Synthesis and Catalysis, Institute of Chemical Sciences and Engineering, Ecole Polytechnique Fédérale de Lausanne (EPFL), EPFL-ISIC-LSCI, BCH 3305, Lausanne, CH 1015 Switzerland.
2. Department of Chemistry, Southern University of Science and Technology, Shenzhen, Guangdong, 518055, China.
3. Laboratory of Renewable Energy Science and Engineering, Institute of Mechanical Engineering, École Polytechnique Fédérale de Lausanne, 1015 Lausanne, Switzerland.

* Corresponding author. E-mail: xile.hu@epfl.ch

Abstract: The reaction of carbon dioxide with hydroxide to form carbonate in near neutral or alkaline medium severely limits the energy and carbon efficiency of CO_2 electroreduction. Here we show that by suppressing the otherwise predominant hydrogen evolution using alkali cations, efficient CO_2 electroreduction can be conducted in acidic medium, overcoming the carbonate problem. The cation effects are general for three typical catalysts including carbon supported tin oxide, gold, and copper, leading to Faradaic efficiency of as high as 90% for formic acid and CO formation. Our analysis suggests hydrated alkali cations physisorbed on the cathode modify the distribution of electric field in the double layer, which impedes hydrogen evolution by suppress the migration of hydronium ions while at the same time promotes CO_2 reduction by stabilizing key intermediates.

Main text: Electrochemical reduction of CO_2 to produce chemicals and fuels is widely studied as a potential solution for renewable energy storage and CO_2 recycling.[1] Because the hydrogen evolution reaction (HER) dominates in acidic aqueous solutions, CO_2 electroreduction is conducted in an alkaline or near neutral medium.[2,3] These reaction media, however, create one of the most important obstacles for high-efficient steady-state CO_2 electrolysis: the facile reaction of CO_2 with hydroxide (OH^-) to form carbonate (CO_3^{2-})[4,5]. In alkaline medium where the overpotentials of many catalysts are minimized thanks to a rate-influencing proton-decoupled one-electron CO_2 reduction step,[6,7] the carbonate problem obliges continuous refreshing of the OH^- electrolytes in a flow-cell configuration in order to obtain a stable performance.[2,3] The regeneration of CO_2 and 2 OH^- from aqueous carbonate is energy demanding and leads to a low or even negative energy efficiency for CO_2 electroreduction.[5] In near neutral media such as bicarbonate solutions, steady-state CO_2 electrolysis is possible.[8,9] However, CO_2 is still consumed by OH^- anions electrochemically generated in CO_2 electroreduction. The (bi)carbonate is protonated near the anode to regenerate CO_2, which leads to a low carbon efficiency.[10] In addition, in near neutral media the high resistance of the solution[11] as well as higher overpotential for oxygen evolution reaction (OER)[12] leads to a high cell voltage and low energy efficiency. In strongly acidic media the resistance and overpotential for OER are lower, and the carbonate problem can be solved since carbonate will not cross the medium to the anode. An acidic medium is also essential to obtain formic acid from CO_2 reduction. In near neutral and alkaline media, the same reduction leads to formate, which requires energy-intensive downstream processes for separation and conversion.

Efficient CO_2 electroreduction in an acidic medium is challenging because the HER is normally more facile than CO_2 reduction. It was reported that in CO_2-saturated 0.1 M $HClO_4$ solutions (pH =1), the Faradaic efficiency of HER was nearly 100% on Fe-N-C[7] and Au[13] catalysts, both of which are efficient CO_2 reduction catalysts in near neutral and alkaline media. The group of Koper showed that CO_2 reduction to CO was feasible in an $HClO_4$-$NaClO_4$ mixed solution with a mild acidity (pH $\geq$ 3). They proposed that the HER was suppressed by OH^- anions generated from CO_2 reduction.[14] During the preparation of our publication, Huang et al. reported efficient CO_2 electroreduction on Cu catalysts in strongly acidic solutions (pH = 0.67) with H_3PO_4-KCl mixed electrolytes.[15] In both studies, alkali cations are essential for CO_2 reduction, but the mechanism of cation-promotion was unclear.

Here we demonstrate efficient CO_2 electroreduction with Faraday efficiency as high as 90% in strongly acidic media (pH =1) by suppressing HER with alkali cations. This approach

can be applied for three representative classes of catalysts, namely carbon supported SnO_2, Au, and Cu nanoparticles (SnO_2/C, Au/C and Cu/C), which give formic acid, CO, and hydrocarbons as main CO_2 reduction products, respectively. Our simulation and analysis indicate that the alkali cations in the double layer of the cathode effectively shield the electric field in the diffusion layer and suppress the migration of hydronium ions towards the cathode, which lowers the concentration of hydronium ions in outer Helmholtz plane (OHP) and thus suppresses HER. Meanwhile the cations strengthen the filed in the Stern layer and stabilizes key intermediates in CO_2 reduction.

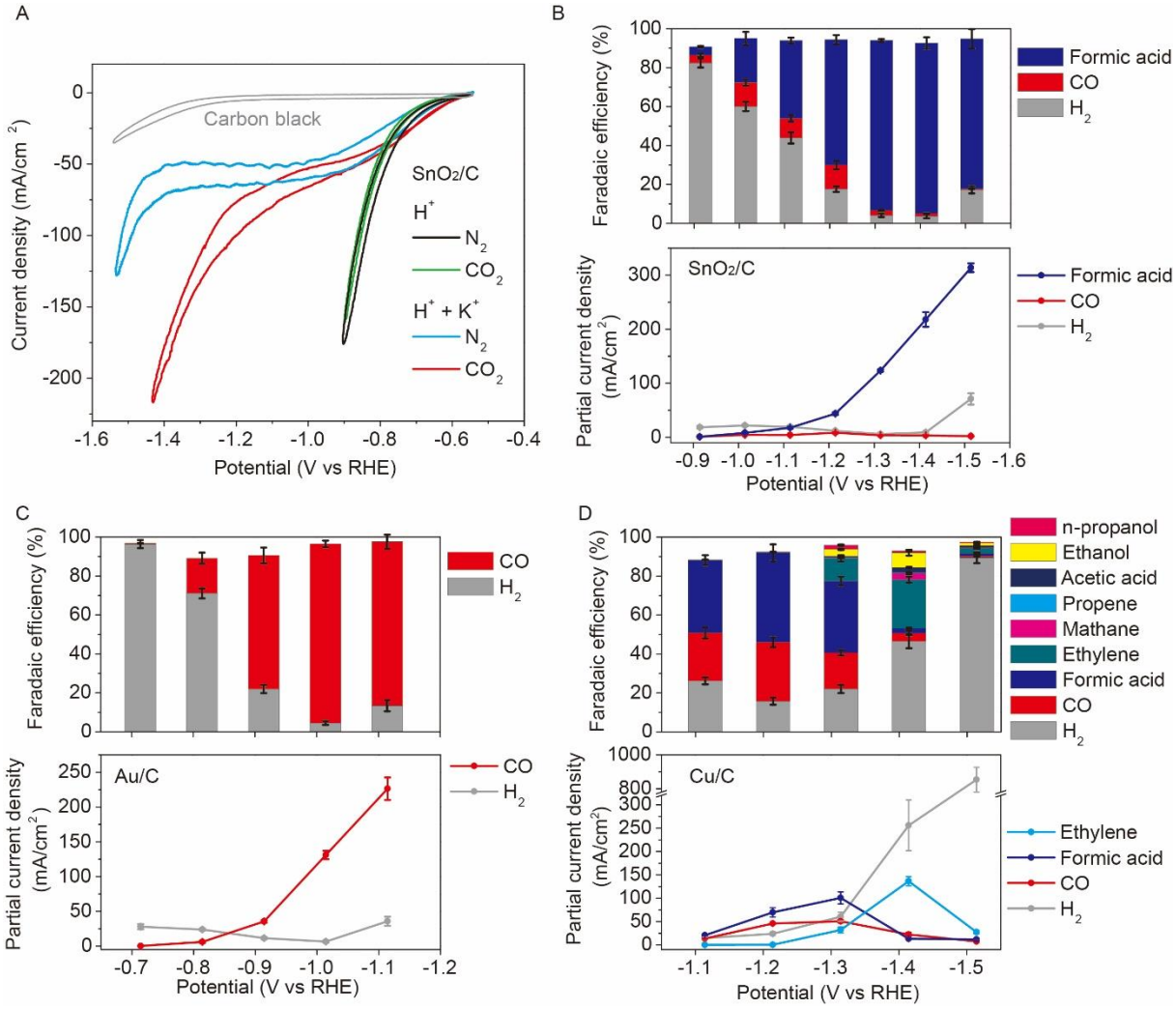

Fig. 1. Performance of CO_2 reduction in acidic solutions containing K^+ ions. (A) CV curves of SnO_2/C in 0.1 M HOTf with N_2 (black) and CO_2 (green), in 0.1 M HOTf + 0.4 M KOTf with N_2 (blue) and CO_2 (red), and CV curve of Vulcan XC-72R in 0.1 M HOTf + 0.4 M KOTf with CO_2 (grey). Scan rate was 20 mV/s. (B-D) Faradaic efficiency (upper) and partial current density (lower) of different reduction products in 0.1 M H_2SO_4 + 0.4 M K_2SO_4. The catalysts were (B) SnO_2/C, (C) Au/C and (D) Cu/C. The partial current densities of minor products on

Cu/C are not shown in the lower part of (D).

The activity and selectivity of the CO_2 reduction reaction are sensitive to alkali metal cations in near neutral bicarbonate solutions.[13,16-19] Several hypotheses such as local pH effect[17] and electrostatic interaction[16,18] have been made to explain these cation effects. Inspired by these studies, we decided to explore a possible influence of alkali cations for CO_2 reduction vis-à-vis the HER in strongly acidic medium. We first probed the effect of K^+ for CO_2 reduction on SnO_2/C at pH = 1. We used a three-electrode flow cell with a gas diffusion electrode (GDE) as working electrode (fig. S2) for electrocatalytic tests. Fig. 1A shows the cyclic voltammetry (CV) curves of SnO_2/C in two different electrolyte solutions: an aqueous solution of 0.1 M trifluoromethanesulfonic acid (HOTf) and a solution containing 0.1 M HOTf + 0.4 M potassium trifluoromethanesulfonate (KOTf). HOTf is a strong acid and the addition of K^+ ions does not change the pH of the solution. The pHs of both solutions are 1. HER was the only reaction under a N_2 atmosphere. The addition of K^+ greatly suppressed the HER as the potential was more negative than -0.8 V vs reversible hydrogen electrode (RHE) (blue and black curves in fig. 1A). In 0.1 M HOTf, the CV curves collected under N_2 and CO_2 were nearly identical, indicating the dominance of HER and the lack of CO_2 reduction in the presence of CO_2. Indeed, H_2 was the only reduction product when CO_2 was present (fig. S3). In the solution containing 0.1 M HOTf plus 0.4 M KOTf, a higher current density was observed in the CV curve with CO_2 at potentials more negative of -1.0 V vs RHE (red curve in fig. 1A). Formic acid and CO were detected as products in this potential range (fig. S3).

We tested the performance of SnO_2/C, Au/C and Cu/C (fig. 1B-D) in electrolyte solutions containing 0.1 M H_2SO_4 + 0.4 M K_2SO_4 (pH = 1.5). This combination of electrolytes is more practical than the combination of HOTf + KOTf, even though addition of K^+ ions slightly changes the pH of H_2SO_4 solutions. For SnO_2/C, formic acid was the major product of CO_2 reduction. The maximum Faradaic efficiency and partial current density were 88% and 314 mA/cm^2, respectively (fig. 1B). These performance metrics are comparable to state-of-the-art results of formic acid production from a solid-state electrolyzer[20] and formate formation in near neutral solutions[21]. Aqueous solution of formic acid could be separated from the electrolyte solution by distillation (fig. S4). This result demonstrated the advantage of an acidic reaction medium for formic acid generation compared to a near neutral or alkaline medium where only formate would be generated. For Au/C, CO was the major product with the maximum Faradaic efficiency and partial current density as 91% and 227 mA/cm^2, respectively (fig. 1C). For Cu/C, formic acid, CO, methane, ethylene, propene, acetic acid, ethanol and 1-propanol were detected

as the products of CO_2 reduction (fig. S5). The minimum Faradaic efficiency of HER was 16%, lower than that of Cu/PFSA catalyst (PFSA = perfluorosulfonic acid) in H_3PO_4-KCl medium (Faradaic efficiency of HER = 36%) reported by Huang et al.[15] Among the products of > 2e reduction, ethylene was the major product with the partial current density of 136 mA/cm^2 (fig. 1D). Its Faradaic efficiency was 25%, similar to the highest Faradaic efficiency for ethylene production on Cu/PFSA in H_3PO_4-KCl medium by Huang et al.[15] The maximum partial current densities of CO formation on Au/C and ethylene formation on Cu/C in acidic media are comparable to those on state-of-the-art catalysts in near neutral and alkaline media.[2,3,22,23]

We also directly compared the performances of Au/C in CO_2 electroreduction in acidic, near neutral (0.8 M $KHCO_3$) and alkaline (0.8 M KOH) media in a two-electrode cell (fig. S6). As expected, the carbonate problem was severe in an alkaline medium. While the initial cell voltage was low, it increased substantially (by 34%) in 2.5 hours (fig. 2A and fig. S6D). Meanwhile, the pH of the solution decreased from 13.5 to 8.1 due to the reaction of OH^- with CO_2 (fig. 2B). In near neutral and acidic media, the cell voltages were largely stable (fig. 2A and fig. S6B-C), as no net reaction between electrolyte and CO_2 occurred in these media. The pHs of the solutions remained stable after 4 h of electrolysis (fig. 2B). The overall cell voltage with the acidic medium was about 0.3 V lower than that with the near neutral medium for 200 mA/cm^2 at 4 h. The potentials vs standard hydrogen electrode (SHE) for the same partial current density of CO on Au/C were within a range of 100 mV at different pH (fig. S7A). However, the equilibrium potential of CO_2/CO vs SHE shifts with 59.2 mV per pH order at 298 K, leading to a higher overpotential in acidic medium than in near neutral and alkaline media (fig. S7B). Similar situations were found for formic acid and ethylene formation on SnO_2/C and Cu/C, respectively (fig. S7C-F). In spite of higher overpotential of CO_2 reduction, the overall cell voltage with acidic medium was still lower than that with near neutral medium, due to lower solution resistance (fig. S8A) and lower overpotential for the OER (fig. S8B).

As mentioned above, even in near neutral medium, carbonate forms from the reaction between CO_2 and OH^- near the cathode, crosses the electrolyte solution, and is protonated near the anode to regenerate CO_2 (fig. S9A). For CO_2 reduction to CO, 50% of CO_2 consumption is captured by the electrolyte to form carbonate.[5] Seger et al. experimentally showed that only 30% of CO_2 consumption was involved in CO_2 reduction when Cu catalyst was used to form deep-reduction products.[10] In our steady state electrolysis in near neutral medium, the amount of CO_2 in the gas mixture generated at the anode compartment was higher than that of O_2 (fig. S9C). In contrast, in acidic medium, release of CO_2 from (bi)carbonate at the anode compartment was

not observed (fig. S9C), indicating no crossover of (bi)carbonate anions through the acidic medium. This result supports the notion that in acidic medium a high carbon efficiency of CO_2 reduction can be achieved by avoiding the carbonate problem.

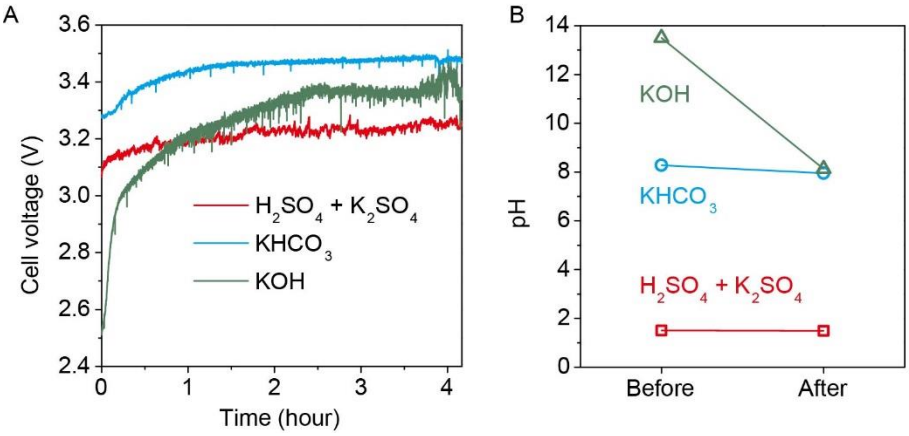

Fig. 2. Comparison of CO_2 electroreduction on Au/C in acidic, near neutral and alkaline media. (A) Cell voltages of two-electrode flow cells with Au/C and IrO_2 as catalysts for cathode and anode, respectively. The current density was 200 mA/cm^2. No *IR* compensation was applied. Electrolytes: 0.1 M H_2SO_4 + 0.4 M K_2SO_4 (red), 0.8 M $KHCO_3$ (blue), and 0.8 M KOH (green). (B) The pH values of electrolyte solutions before and after electrolysis.

To understand how K^+ further suppressed HER on SnO_2, Au and Cu in strongly acidic solutions, we measured linear sweeping voltammetry (LSV) curves of a polycrystalline Au rotating disk electrode (RDE) in different electrolyte solutions (fig. 3A). The onset potential of HER in 0.1 M HOTf + 0.4 M KOTf is close to that in HOTf solution (0.1 M or 0.5 M), while in the K^+-containing solution, a plateau of current density appears from -0.6 V vs SHE. The current density increases again at -1.3 V vs SHE, close to the onset potential of HER in 0.4 M KOTf, indicating reduction of water molecules starts at this potential. The plateau is about 6% higher than the limiting diffusion current density of hydronium reduction calculated according to the Levich equation. In sharp contrast, in 0.1 M HOTf, no plateau corresponding to the diffusion limitation of hydronium reduction was observed. LSV curves of SnO_2/C on glassy carbon RDE (fig. S10A-C) and CV curves of SnO_2/C on GDE in N_2 atmosphere (fig. 1A) show similar trends to curves in fig. 3A, indicating the suppression of HER by K^+ in strongly acidic medium is a universal effect.

We next probed whether other alkali cations such as Li^+, Na^+ and Cs^+ have the similar effect on the competition between HER and CO_2 reduction as K^+. Indeed, in 0.1 M HOTf + 0.4 M MOTf (M = Li, Na, Cs), plateaus of current densities corresponding to the diffusion-limited

reduction of hydronium ions were observed (fig. S10D-F), indicating that these alkali cations also suppressed the migration of hydronium ions. We then measured CO_2 electroreduction on SnO_2/C and Cu/C in acidic solutions containing these alkali cations (fig. S11-S13). All alkali cations promoted CO_2 reduction by inhibiting HER, but the effects are variable. On SnO_2/C the Faradaic efficiency of CO_2 reduction increased in the order Li < Na < K < Cs for both catalysts (fig. 3B), and the partial current densities of formic acid and CO increased in the same order (fig. 3C). On Cu/C the partial current density of ethylene increased in a similar order of Li < Na < K ≈ Cs (fig. S13).

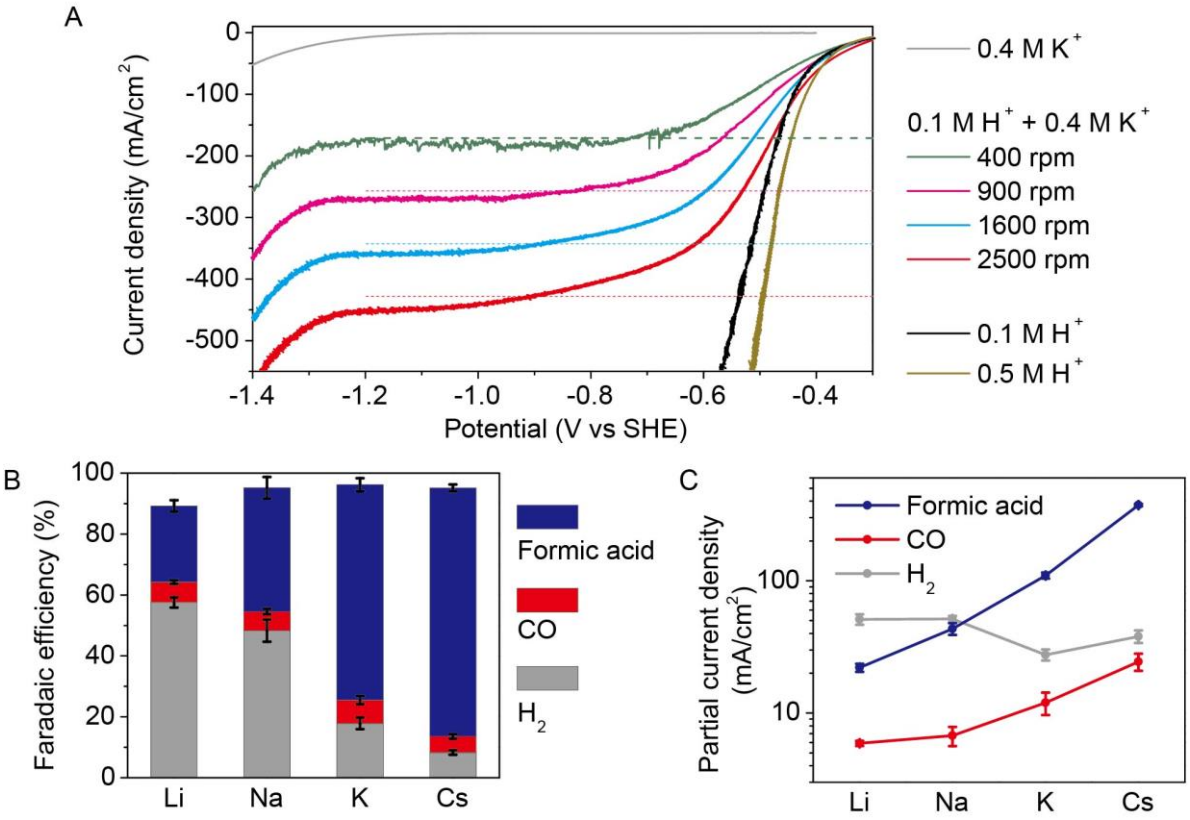

Fig. 3. Cation effects on HER and CO_2 reduction. (A) LSV curves of Au RDE in N_2 saturated solutions: 0.1 M HOTf + 0.4 M KOTf (green, pink, blue and red curves were collected with the rotating speed of 400, 900, 1600, and 2500 rpm, respectively), 0.4 M KOTf (gray, 1600 rpm), 0.1 M HOTf (black, 1600 rpm) and 0.5 M HOTf (brown, 1600 rpm). The horizontal dashed lines indicate the limiting diffusion current densities of the reduction of hydronium ions at the corresponding rotating speed calculated from the Levich equation. (B) Faradaic efficiency and (C) partial current densities of formic acid, CO and H_2 of SnO_2/C in 0.1 M HOTf + 0.4 M MOTf (M = Li, Na, K and Cs) at -1.34 V vs RHE.

In the study of Huang et al on CO_2 reduction in strongly acidic medium with Cu

catalysts,[15] they proposed that a high cathodic current density would lead to hydronium depletion and pH increase near the cathode. Water instead of hydronium reduction then contributes to the majority of HER currents. Alkali cations were then proposed to favor CO_2 reduction over water reduction, although the details of this promotion were not studied. This mechanistic hypothesis does not take into account the migration of hydronium ions under an electric field during HER. It cannot explain why in alkali cation-free solutions the HER current density can exceed the diffusion limit of hydronium ions and why the addition of alkali cations can suppress the HER current density to a limiting value, as observed in our study.

To probe how alkali cations suppressed the reduction of hydronium ions, we conducted a simulation based on the Poisson-Nernst-Planck model (PNP) which includes migration as one of the mechanisms for mass tranport.[24] Hydronium ions, K^+ and OTf^- were considered, and the reduction of hydronium ions was regarded as the only source of HER in strongly acidic media. The HER current density was assumed proportional to the concentration of hydronium ions in the OHP and exponential to the electrode potential. The simulation reproduced the features of HER at potentials more positive than the onset of reduction of water (fig. S14): in a K^+-free solution, the current density of hydronium reduction increased without any limitation as potential went cathodically; in a K^+-containing solution, a plateau of current density higher than the limiting diffusion current density based on the Levich equation was observed.

Fig. 4A and B show the profiles of potential and electric field strength with and without K^+ ions. The addition of K^+ ions led to a stronger electric field in the Stern layer and a weaker electric field at >2 nm away from the cathode (inset of fig. 4B). These effects were due to the accumulation of K^+ ions at OHP. The electric fields generated by cathode and by K+ ions at OHP were in the same direction in the Stern layer while they were opposite in the diffuse layer (fig. 4C). Although hydronium ions accumulated at OHP had a similar effect to K^+ on the electric field distribution, the effect was weak since hydronium ions at OHP were consumed in HER (fig. 4D). Hence, in K^+-free medium, the electric field was not sufficiently confined within a few nm from the cathode and the migration of hydronium ions under electric field facilitated the refilling of hydronium ions to OHP. The concentration of hydronium ions at OHP did not change significantly as the electrode potential shifted cathodically (fig. S15A-B), indicating hydronium ions would not be depleted as current density increased. In K^+-containing medium, in sharp contrast, the concentration of hydronium ions at OHP decreased as the electrode potential was more negative (fig. S15C), indicating only in an alkali cation-containing medium, depletion of hydronium ions near the cathode would occur.

For CO_2 reduction in aqueous media, the adsorbed CO_2 (CO_{2ad}) is regarded as a key intermediate.[7,25] Stabilization of CO_{2ad} on the surface of catalysts promotes the production of CO and formate.[22,26,27] The two C=O bonds of CO_{2ad} bend away from the surface, endowing CO_{2ad} with a large dipole moment oriented outwards.[16,28] Thus, the electric field in Stern layer stabilizes CO_{2ad} (fig. 4D). Similarly, OCCO intermediate, a key intermediate for the formation of ethylene and ethanol on Cu-based catalyst, has a large outwards dipole moment[16,29] and is stabilized by the electric field in Stern layer. Therefore, K^+ ions not only suppressed HER by impeding the migration of hydronium ions in the diffuse layer, but also promoted CO_2 electroreduction due to the interaction between electric field and dipole moment of adsorbed intermediates.

The effect of different alkali cations can also be explained by the model in fig.4C. The size of hydrated alkali cations decreased from Li to Cs. As the size of hydrated cations decreases, more alkali cations can accumulate in the OHP,[16] leading to a stronger electric field in Stern layer and a weaker electric field in diffuse layer.[30] This explains how the size of hydrated alkali cations affects the competition between HER and CO_2 reduction in strongly acidic media.

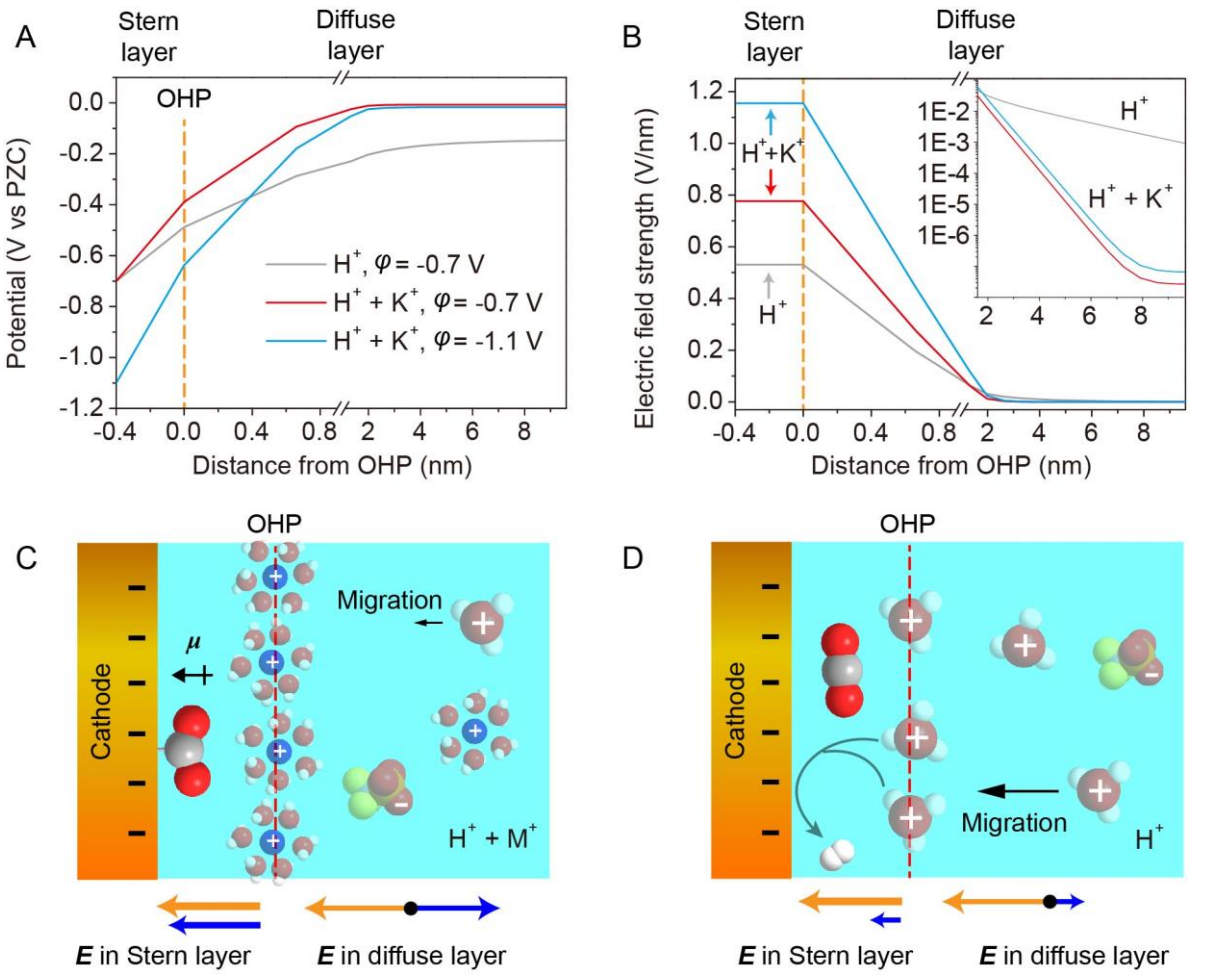

Fig. 4. Cation effects on electric field distribution. Simulated (A) potential and (B) electric field strength profiles over the distance from the cathode. The direction of electric field was towards the cathode. The surface of electrode was at x = -0.4 nm. The orange dashed lines at x = 0 nm represent OHP. Gray curves show the profiles of 0.1 M HOTf with the electrode potential of -0.7 V vs potential of zero charge (PZC). Red and blue curves show the profiles of 0.1 M HOTf + 0.4 M KOTf with the electrode potential of -0.7 V and -1.1 V vs PZC, respectively. The rotating speed was 400 rpm in the simulation. At -1.1 V vs PZC, the HER current density reached the plateau. The inset of panel (B) shows the magnification of the electric field strength profile between 1.6 nm and 9.6 nm. Schemes of double layer near cathode in (C) HOTf + MOTf and (D) HOTf media. Grey, red, white, blue, yellow and orange balls represent C, O, H, K, F and S atoms, respectively. Orange arrows represent electric field (E) generated by the cathode and blue arrows represent E generated by cations at OHP. In panel (C), μ represent the dipole moment of adsorbed CO_2 intermediate. In panel (D), hydronium ions at OHP are consumed by HER.

It is noteworthy that the partial current density of CO_2 reduction could significantly exceed the diffusion limitation of hydronium ions in the presence of K^+ (fig. S16), implying that water molecules are the proton source for CO_2 reduction. Thus, CO_2 reduction leads to the formation of OH^- ions, which further react with hydronium ions near the electrode and suppress HER.[14,31] Due to this effect, Faradaic efficiency of CO_2 reduction reached 90% for SnO_2/C and Au/C catalysts (fig. 1B-C).

In summary, by using alkali cations to suppress hydronium reduction and promote CO_2 reduction, we demonstrated efficient CO_2 electroreduction in strongly acidic medium. We showed that this approach is universal for various catalysts and cations, and we revealed cation-induced modulation of electric field as the origin of the cation effects. This work provides a promising strategy to avoid the carbonate problem in CO_2 electroreduction, which is one of the main road blockers for low-temperature CO_2 electrolysis.

ACKNOWLEDGMENTS

The authors thank Dr. Lichen Bai for the help in TEM characterizations. **Funding:** This work was supported by the European Research Council (no. 681292), NCCR Catalysis, a National Centre of Competence in Research funded by the Swiss National Science Foundation, the EPFL, the European Union Marie Sklodowska-Curie Individual Fellowships (No. 891545-

ADBCRZB to W.R.), the European Union's Horizon 2020 research and innovation programme under grant agreement No 85144 (SELECT-CO2), and a Starting Grant of the Swiss National Science Foundation No. 155876 (SCOUTS). **Author contribution:** J.G. performed the majority of the synthesis, characterization, and electrochemical tests. S.L. performed the simulations. W.N. performed the Au rotating disk electrode tests. W.R. performed the electrochemical tests in near neutral and alkaline media. J.G., S.L., S.H. and X.H. analyzed the data. J.G. and X.H. wrote the paper, with input from all other co-authors. S.H. and X.H. directed the research.

Competing interests: The authors declare no competing interests.

Data and materials availability: All data are reported in the main text and supplementary information.

REFERENCES

1 Chu, S., Cui, Y. & Liu, N. The path towards sustainable energy. *Nature Materials* **16**, 16-22, (2017).

2 Verma, S. *et al.* Insights into the Low Overpotential Electroreduction of CO2 to CO on a Supported Gold Catalyst in an Alkaline Flow Electrolyzer. *ACS Energy Letters* **3**, 193-198, (2018).

3 Dinh, C.-T., García de Arquer, F. P., Sinton, D. & Sargent, E. H. High Rate, Selective, and Stable Electroreduction of CO2 to CO in Basic and Neutral Media. *ACS Energy Letters* **3**, 2835-2840, (2018).

4 Zhang, B. A., Ozel, T., Elias, J. S., Costentin, C. & Nocera, D. G. Interplay of Homogeneous Reactions, Mass Transport, and Kinetics in Determining Selectivity of the Reduction of CO2 on Gold Electrodes. *ACS Central Science* **5**, 1097-1105, (2019).

5 Rabinowitz, J. A. & Kanan, M. W. The future of low-temperature carbon dioxide electrolysis depends on solving one basic problem. *Nature Communications* **11**, 5231, (2020).

6 Wuttig, A., Yaguchi, M., Motobayashi, K., Osawa, M. & Surendranath, Y. Inhibited proton transfer enhances Au-catalyzed CO2-to-fuels selectivity. *Proceedings of the National Academy of Sciences* **113**, E4585-E4593, (2016).

7 Varela, A. S. *et al.* pH Effects on the Selectivity of the Electrocatalytic CO2 Reduction on Graphene-Embedded Fe–N–C Motifs: Bridging Concepts between Molecular Homogeneous and Solid-State Heterogeneous Catalysis. *ACS Energy Letters* **3**, 812-817, (2018).

8 Hori, Y. in *Modern Aspects of Electrochemistry* (eds Constantinos G. Vayenas, Ralph E. White, & Maria E. Gamboa-Aldeco) 89-189 (Springer New York, 2008).

9 Zhu, D. D., Liu, J. L. & Qiao, S. Z. Recent Advances in Inorganic Heterogeneous Electrocatalysts for Reduction of Carbon Dioxide. *Advanced Materials* **28**, 3423-3452, (2016).

10 Ma, M. *et al.* Insights into the carbon balance for CO2 electroreduction on Cu using gas diffusion electrode reactor designs. *Energy & Environmental Science* **13**, 977-985, (2020).

11 Wang, J., Xu, F., Jin, H., Chen, Y. & Wang, Y. Non-Noble Metal-based Carbon Composites in Hydrogen Evolution Reaction: Fundamentals to Applications. *Advanced Materials* **29**, 1605838,

(2017).
12 Shao, Y., Xiao, X., Zhu, Y.-P. & Ma, T.-Y. Single-Crystal Cobalt Phosphate Nanosheets for Biomimetic Oxygen Evolution in Neutral Electrolytes. *Angewandte Chemie International Edition* **58**, 14599-14604, (2019).
13 Ringe, S. *et al.* Double layer charging driven carbon dioxide adsorption limits the rate of electrochemical carbon dioxide reduction on Gold. *Nature Communications* **11**, 33, (2020).
14 Bondue, C. J., Graf, M., Goyal, A. & Koper, M. T. M. Suppression of Hydrogen Evolution in Acidic Electrolytes by Electrochemical CO2 Reduction. *Journal of the American Chemical Society* **143**, 279-285, (2021).
15 Huang, J. E. *et al.* CO2 electrolysis to multicarbon products in strong acid. *Science* **372**, 1074-1078, (2021).
16 Resasco, J. *et al.* Promoter Effects of Alkali Metal Cations on the Electrochemical Reduction of Carbon Dioxide. *Journal of the American Chemical Society* **139**, 11277-11287, (2017).
17 Singh, M. R., Kwon, Y., Lum, Y., Ager, J. W. & Bell, A. T. Hydrolysis of Electrolyte Cations Enhances the Electrochemical Reduction of CO2 over Ag and Cu. *Journal of the American Chemical Society* **138**, 13006-13012, (2016).
18 Ringe, S. *et al.* Understanding cation effects in electrochemical CO2 reduction. *Energy & Environmental Science* **12**, 3001-3014, (2019).
19 Zhang, F. & Co, A. C. Direct Evidence of Local pH Change and the Role of Alkali Cation during CO2 Electroreduction in Aqueous Media. *Angewandte Chemie International Edition* **59**, 1674-1681, (2020).
20 Xia, C. *et al.* Continuous production of pure liquid fuel solutions via electrocatalytic CO2 reduction using solid-electrolyte devices. *Nature Energy* **4**, 776-785, (2019).
21 Liu, L.-X. *et al.* Tuning Sn3O4 for CO2 reduction to formate with ultra-high current density. *Nano Energy* **77**, 105296, (2020).
22 Gu, J., Hsu, C.-S., Bai, L., Chen, H. M. & Hu, X. Atomically dispersed Fe³⁺ sites catalyze efficient CO2 electroreduction to CO. *Science* **364**, 1091-1094, (2019).
23 Li, F. *et al.* Molecular tuning of CO2-to-ethylene conversion. *Nature* **577**, 509-513, (2020).
24 Newman, J. & Thomas-Alyea, K. E. *Electrochemical Systems*. 3rd edn edn, (John Wiley & Sons, 2004).
25 Wuttig, A., Yoon, Y., Ryu, J. & Surendranath, Y. Bicarbonate Is Not a General Acid in Au-Catalyzed CO2 Electroreduction. *Journal of the American Chemical Society* **139**, 17109-17113, (2017).
26 Chen, Y., Li, C. W. & Kanan, M. W. Aqueous CO2 Reduction at Very Low Overpotential on Oxide-Derived Au Nanoparticles. *Journal of the American Chemical Society* **134**, 19969-19972, (2012).
27 Zhang, S., Kang, P. & Meyer, T. J. Nanostructured Tin Catalysts for Selective Electrochemical Reduction of Carbon Dioxide to Formate. *Journal of the American Chemical Society* **136**, 1734-1737, (2014).
28 Chen, L. D., Urushihara, M., Chan, K. & Nørskov, J. K. Electric Field Effects in Electrochemical CO2 Reduction. *ACS Catalysis* **6**, 7133-7139, (2016).
29 Sandberg, R. B., Montoya, J. H., Chan, K. & Nørskov, J. K. CO-CO coupling on Cu facets: Coverage, strain and field effects. *Surface Science* **654**, 56-62, (2016).
30 Bohra, D., Chaudhry, J. H., Burdyny, T., Pidko, E. A. & Smith, W. A. Modeling the electrical double layer to understand the reaction environment in a CO2 electrocatalytic system. *Energy & Environmental Science* **12**, 3380-3389, (2019).
31 Grozovski, V., Vesztergom, S., Láng, G. G. & Broekmann, P. Electrochemical Hydrogen Evolution: H+or H2O Reduction? A Rotating Disk Electrode Study. *Journal of The Electrochemical Society* **164**, E3171-E3178, (2017).

Material synthesis

Chemicals: Carbon black (Vulcan XC-72R), anhydrous tin(II) chloride ($SnCl_2$, 98%, Acros), sodium oxalate ($Na_2C_2O_4$, 99.5%, Sigma-Aldrich), hydrochloric acid (HCl, 37%, VWR international SA), gold(III) chloride hydrate ($HAuCl_4 \cdot xH_2O$, 99.999%, Sigma-Aldrich), oleylamine (approximate C18-content 80-90%, Acros), borane tert-butylamine complex (BTB, 97%, Sigma-Aldrich), copper(II) acetylacetonate ($Cu(acac)_2$, 98%, Acros) and trioctylphosphine oxide (TOPO, 99%, Sigma-Aldrich) were used as received without further purification. Deionized water (18 MΩ·cm) obtained from a Milli-Q integral water purification system (Merck Millipore Corporation) was used for all experiments.

Synthesis of SnO_2/C: SnO_2/C was synthesized by a method modified from literature [1]. Carbon black was first treated with nitric acid: 50 mg of carbon black was dispersed in 30 mL of nitric acid (HNO_3, 65%, Merck) and kept at 80 °C for 12 hours. Then, the carbon black was collected by centrifugation and washed by deionized water until the supernatant was neutral. Finally, the carbon black was dried under vacuum. SnC_2O_4/C, the precursor of SnO_2/C, was then synthesized: 120 mg of nitric acid-treated carbon black was dispersed in 10 mL of deionized water, and 200 μL of HCl (37%) was added. 190 mg of anhydrous $SnCl_2$ was added into the dispersion under vigorous stirring. After 30 seconds, 10 mL of 0.2 M $Na_2C_2O_4$ solution was added quickly and the dispersion was kept under stirring at 25 °C for 30 minutes. SnC_2O_4/C was then collected by centrifugation, washed by deionized water for three times, and dried under vacuum at 25 °C. The as-synthesized SnC_2O_4/C was then loaded in a corundum crucible and put into a muffle. The sample was heated to 400 °C in air with a ramping rate of 5 °C/min, and kept at 400 °C for 4 hours. After the sample cooled naturally to room temperature, SnO_2/C was obtained. Fig. S1A and S1B show the HAADF-STEM image and PXRD pattern of SnO_2/C.

Synthesis of Au/C: Au/C was synthesized with a method modified from literature [2]. 50 mg of $HAuCl_4 \cdot xH_2O$, 125 μL of toluene and 30 mg of carbon black were added

into 10 mL of oleylamine, and the mixture was stirred at 600 rpm for 10 minutes under N_2 atmosphere. 22.5 mg of BTB was dissolved in 2.5 mL of oleylamine and this solution was rapidly injected into the above-mentioned mixture. The resulting mixture was stirred at 25 °C under N_2 for 1 hour. Then, 15 mL of ethanol was added into the mixture. A black powder was separated from the reaction mixture by centrifugation, washed by toluene-ethanol mixed solvent (v:v = 1:1) twice, and dried at 70 °C. Finally, the powder was heated at 185 °C in air overnight to give the final sample of Au/C. Fig. S1C and S1D show the HAADF-STEM image and PXRD pattern of Au/C.

Synthesis of Cu/C: Cu/C was synthesized with a method modified from literature [3]. 0.196 g of $Cu(acac)_2$ and 2.90 g of TOPO were dissolved in 35 mL of oleylamine and 100 mg of carbon black was added into this solution. The mixture was evacuated at 80 °C for 15 minutes, and then rapidly heated to 200 °C under N_2 atmosphere. The reaction was kept at 200 °C for 1 hour and then cooled to room temperature naturally. 40 mL of ethanol was then added into the mixture and a black solid was separated from the reaction mixture by centrifugation. This crude product was washed with *n*-hexane-ethanol mixed solvent (v:v = 1:1) twice, and dried under vacuum at room temperature to give the final sample of Cu/C. Cu/C was stored in glove box with N_2 to prevent the oxidation of Cu. Fig. S1E and S1F show the HAADF-STEM image and PXRD pattern of Cu/C.

Characterization

Powder X-ray diffraction (PXRD) patterns were collected on an Aeris diffractometer (PANalytical) with monochromatic Cu Kα radiation. The contribution of Cu Kα2 radiation was subtracted.

High angle annular dark field-scanning transmission electron microscopy (HAADF-STEM) images were collected on an FEI Talos TEM operated at 200 kV with high brightness XFEG gun. To prepare the sample, 1 mg of catalyst was dispersed in 1 mL of ethanol, and 5 μL of the dispersion was dropped onto a grid covered by ultrathin

carbon membrane. For SnO_2/C and Au/C, Cu grids were used. For Cu/C, Au grid was used.

Electrochemical measurements

General: All electrochemical measurements were carried out on a Gamry Reference 3000 electrochemical instrument. Current-interrupt *IR* compensation was used unless otherwise noted. Ag/AgCl | saturated KCl electrode was used as the reference electrode. Potential of working electrode versus SHE was calculated according to:

E(vs SHE) = E(vs Ag/AgCl) + 0.197 V

Potential versus RHE was calculated according to:

E(vs RHE) = E(vs SHE) + 0.0592 V × pH

The pH value of electrolyte was measured by pH meter (HI 991002, Hanna instruments).

Electrolyte solutions: Deionized water was used for the preparation of electrolyte solutions. Sulfuric acid (H_2SO_4, 95%, Merck), lithium sulfate (Li_2SO_4, 99%, Roth), sodium sulfate decahydrate ($Na_2SO_4 \cdot 10H_2O$, 99%, Sigma-Aldrich) and potassium sulfate (K_2SO_4, 99%, ABCR) were used to prepare solutions of 0.1 M H_2SO_4 and 0.1 M H_2SO_4 + 0.4 M M_2SO_4 (M = Li, Na and K). Sulfuric acid and cesium hydroxide monohydrate ($CsOH \cdot H_2O$, 99%, Sigma-Aldrich) were used to prepare solution of 0.1 M H_2SO_4 + 0.4 M Cs_2SO_4. Trifluoromethanesulfonic acid (HOTf, 99%, Fluorochem), lithium trifluoromethanesulfonate (LiOTf, 98%, Acros), sodium trifluoromethanesulfonate (NaOTf, 98%, Acros) and potassium trifluoromethanesulfonate (KOTf, 99%, Fluorochem) were used to prepare solutions of 0.1 M HOTf and 0.1 M HOTf + 0.4 M MOTf (M = Li, Na and K). HOTf and cesium hydroxide monohydrate were used to prepare solution of 0.1 M HOTf + 0.4 M CsOTf. Potassium bicarbonate (KHCO3, 99.7%, Sigma-Aldrich) was used to prepare 0.8 M $KHCO_3$. Potassium hydroxide (KOH, 1 mol/L solution, Merck) was used to prepare 0.8 M KOH.

Three-electrode flow cell: Fig. S2 shows the scheme of this cell. The left part,

made of stainless steel, was used as the current collector of the working electrode and the gas chamber of CO_2 stream behind GDE. The two PEEK parts were the chambers for electrolyte solutions for the working and counter electrodes. The window for the effective area was set to 1 cm × 1 cm. The thickness of each chamber was 1 cm. Each chamber has an inlet and an outlet for electrolyte. The reference electrode was inserted in the chamber of the working electrode. Nafion® 211 membrane was used to separate the counter electrode from the chamber of the working electrode. Titanium plate with a window (1 cm × 1 cm) was used as the current collector for the counter electrode. PTFE films were used as gaskets. All parts were pressed together by four sets of screws and nuts.

Preparation of electrodes: To prepare the catalyst ink of SnO_2/C, Au/C and Cu/C, 20 mg of catalyst, 4 mL of ethanol and 200 μL of Nafion® dispersion (5%, ABCR) were mixed and sonicated for 30 minutes. CeTech carbon cloth with a micropore layer on one side (W1S1009) was used as the GDE. The carbon cloth was cut into 3 cm × 3 cm square, mounted on a vertically placed heating plate and heated to 120 °C. The ink was sprayed onto the micropore-layer side of the carbon cloth by air-brush. The carbon cloth was then cut into 4 pieces (1.5 cm × 1.5 cm) as the working electrodes. Iridium(IV) oxide (IrO_2, 99%, ABCR) was used as the catalyst for the counter electrode. The ink of IrO_2 containing 20 mg of IrO_2, 4 mL of ethanol, and 40 μL of Nafion® dispersion. ELAT hydrophilic carbon cloth and CeTech W1S1009 carbon cloth were used for the counter electrode for the three-electrode and two-electrode flow cells, respectively. The counter electrode was prepared with the same spraying method as the working electrode. When we tested Cu/C in 0.1 M H_2SO_4 + 0.4 M K_2SO_4 and 0.1 M H_2SO_4 + 0.4 M Cs_2SO_4, half of the electrode was covered by Kapton tape and the effective area of the electrode was 0.5 cm^2. The effective area of electrode in all the other cases was 1 cm^2.

Potential dependent performance test: The potential dependent CO_2 reduction properties were tested in the three-electrode flow cell with chronoamperometry method. The volumes of both catholyte and anolyte solutions were 14 mL, and both of them were circulated with a flow rate of 5 mL/min. The flow rate was controlled by a

peristaltic pump (REGLO Digital MS-4/8, Ismatec). The humidified CO_2 was connected to the inlet of the gas chamber and the outlet was connected to GC for online detection of gas-phase products. The flow of CO_2 was controlled by a mass flow controller (Red-y smart series, Vögtlin) in the range ≤ 50 standard cubic centimeters per minute (sccm) and by another mass flow controller (EL-FLOW, Bronkhorst) in the range between 50 and 200 sccm. The flow rate of CO_2 was adjusted according to current as shown in Fig. S5A. The duration of one chronoamperometry test was 30 minutes. The online GC sampling was at 10 minutes. 400 μL of electrolyte solution was taken after each chronoamperometry test for ^{1}H-NMR test to quantify the products dissolved in electrolyte. Current densities were averaged over 30 minutes. The error bars of Faradaic efficiency and partial current density were standard deviations based on tests of 3 individual working electrodes.

Detection of products: Gas phase products were detected online by gas chromatography (GC). H_2 and CO were detected by a homemade GC equipped with a Carboxen®-1010 PLOT capillary column and a thermal conductivity detector (TCD, VICI). Helium was used as the carrier gas for the analysis of CO and argon was used for the analysis of H_2. The temperature program was: keeping at 35 °C for 3 minutes; heating to 80 °C with a ramping rate of 20 °C/min; keeping at 80 °C for 5 minutes.

Methane, ethylene and propene were detected by a Claurus 400 GC (Perkin Elmer) equipped with a Porapak Q column (Agilent) and a flame ionization detector (FID). H_2 was used as the carrier gas. The temperature program was: keeping at 50 °C for 5 minutes; heating to 150 °C with a ramping rate of 20 °C/min; keeping at 150 °C for 10 minutes.

^{1}H-nuclear magnetic resonance (^{1}H-NMR, 400 MHz, Bruker) was used to detect the solution phase products after chronoamperometry tests. Dimethyl sulfoxide (DMSO) was used as an inner standard to quantify the products. 30.7 μL of DMSO dissolved in 70 mL of deionized water was used as the standard solution (6.17 mmol/L). For each test, 400 μL of the electrolyte for working electrode, 40 μL of DMSO standard solution

and 50 μL of deuterium oxide (D_2O) were mixed.

Fig. S5B-E show the GC-TCD curves with He and Ar as the carrier gas, the GC-FID curve, and the ^{1}H-NMR spectrum of catholyte for Cu/C, respectively. The electrolyte was 0.1 M H_2SO_4 + 0.4 M K_2SO_4. The chronoamperometry test was conducted at -1.41 V vs RHE for 30 minutes.

Calculation of Faradaic efficiency and partial current density: The Faradaic efficiency of a gas product *g* was calculated according to the equation:

$$\mathrm{FE}_g = \frac{N_g \cdot r_g \cdot F}{I} = \frac{N_g p f x_g F/RT}{I} \qquad \text{(S1)}$$

In this equation, N_g is the number of electrons transferred to produce one molecule of *g*. For H_2, CO, methane, ethylene and propene, N_g equals 2, 2, 8, 12 and 18, respectively. r_g is the formation rate of *g* (unit: mol/s). *F* is the Faraday constant (9.65×10^4 C/mol). *I* is current. x_g is the fraction of gas *g* detected by GC. *f* is the mass flow rate of gas flow (unit: sccm). *p* is 101 kPa and T is 273 K. *R* is the gas constant (8.314 $J \cdot mol^{-1} \cdot K^{-1}$).

The Faradaic efficiency of a solution-phase product *s* was calculated according to the equation:

$$\mathrm{FE}_s = \frac{N_s \cdot n_s \cdot F}{Q} = N_s \cdot \frac{6 \cdot c_{\mathrm{DMSO}} \cdot V_{\mathrm{DMSO}} \cdot A_{s,H}}{N_{s,H}} \cdot \frac{V_{\mathrm{ele}}}{V_{\mathrm{NMR}}} \cdot F/Q \qquad \text{(S2)}$$

In this equation, N_s is the number of electrons transferred to produce one molecule of *s*. For formic acid, acetic acid, ethanol and 1-propanol, N_s equals 2, 8, 12 and 18, respectively. n_s is the total amount of *s* generated in one chronoamperometry test (unit: mol). *Q* is the integrated charge of one test (unit: C). c_{DMSO} is the concentration of DMSO in standard solution (6.17 mmol/L) and V_{DMSO} is the volume of standard solution (40 μL). $A_{s,H}$ is the relative area of the peak in ^{1}H-NMR spectrum used for quantification of *s* with respect to the peak of 6 H atoms of DMSO. For ethanol and 1-propanol, the peaks of methyl groups were used for quantification. $N_{s,H}$ is the number of H atoms in one *s* molecule used for quantification. For formic acid, acetic acid, ethanol and 1-propanol, $N_{s,H}$ equals 1, 3, 3 and 3, respectively. V_{ele} is the volume of

electrolyte for working electrode and V_{NMR} is the volume of electrolyte used for NMR test.

The partial current density of product *p* was calculated according to the equation:

$$j_p = j \cdot FE_p \quad \text{(S3)}$$

In this equation, *j* is the current density normalized to the area of working electrode.

Production of aqueous solution of pure formic acid: SnO_2/C was used as the catalyst in the three-electrode cell. Nafion® 211 and Fumasep® FAA-3-50 membranes were used for 0.1 M H_2SO_4 + 0.4 M K_2SO_4 and 0.8 M $KHCO_3$, respectively. The volumes of both catholyte and anolyte solutions were 10 mL, and both of them were circulated with a flow rate of 5 mL/min. Chronoamperometry tests at -1.5 V vs SHE for 15000 seconds were conducted, as shown in fig. S4. After the electrolysis, the volume of the electrolyte for working electrode was adjusted to 10 mL by adding deionized water. 40 μL of this electrolyte, 40 μL of DMSO standard solution, 50 μL of D_2O and 360 μL of deionized water were mixed for ^{1}H-NMR test. The electrolyte solution was then loaded in a 25-mL flask and heated by an oil bath at 150 °C. The distillate was collected until all the water in the flask was evaporated. The volume of the distillate was adjusted to 10 mL by adding deionized water and the sample for ^{1}H-NMR test was prepared with the same method.

Two-electrode flow cell: Fig. S6 shows the scheme of the two-electrode flow cell. CeTech W1S1009 carbon cloths were used as both cathode and anode. Au/C and IrO_2 were used as catalysts for cathode and anode, respectively. Titanium plate was used as current collector for both electrodes. An EPDM plate with the thickness of 1.5 mm was used as the chamber of electrolyte solution. The effective window for electrolysis was a circle with the diameter of 1.13 cm (area = 1 cm^2). Kapton tapes with circular windows with the same size was pasted on both electrodes to control the effective area exposed to the electrolyte. No membrane was used between cathode and anode and two electrodes shared the same electrolyte. CO_2 and He streams were supplied behind cathode and anode, respectively. The volume of electrolyte solution was 10 mL, which

was circulated with the flow rate of 1 mL/min. For each kind of electrolyte, chronopotentiometry test at 200 mA/cm^2 was conducted for 15000 seconds. No *IR* compensation was used when recording the cell voltage. The flow rates of CO_2 and He were 100 sccm and 6 sccm, respectively. CO was detected by online GC analysis. The electrochemical impedance spectroscopy tests were conducted at open circuit potential with an amplitude of 10 mV from 300 kHz to 0.1 Hz.

Rotating disk electrode experiments: The RDE (Autolab) has a glassy carbon disk with a diameter of 5 mm. Before experiments, the electrode was polished by alumina polishing powder (0.05 μm). To prepare the catalyst ink, 5 mg of SnO_2/C, 1 mL of deionized water, 250 μL of isopropanol, and 50 μL of Nafion® dispersion were mixed and sonicated for 30 minutes. 20 μL of the ink was drop-cast on the RDE and dried under N_2 flow. The tests were conducted in a three-neck flask. The RDE was inserted inclinedly from the right side of the flask, facilitating the bubbles generated on the RDE to escape (fig. S17 and movie S1). The reference electrode was put in a Luggin capillary and the distance between the tip of the capillary and RDE was 5 mm. A platinum wire was used as the counter electrode. The electrolyte was saturated with N_2. Linear sweeping voltammetry curves were collected with a scan rate of 5 mV/s. The resistance of electrolyte was determined by high-frequency impedance measurements and *IR* compensation was done after experiment.

The limiting diffusion current density of the reduction of hydronium ions was calculated according to Levich equation [4] (dashed horizontal lines in fig. 3A and fig. S9):

$$j_{d,H^+} = 0.62FD_{H^+}^{2/3}\nu^{-1/6}c_{0,H^+}\omega^{1/2} \quad \text{(S4)}$$

In this equation, F is the Faraday constant (9.65 × 10^4 C/mol), D_{H+} is the diffusion coefficient of hydronium ions (9.3 × 10^{-5} cm^2/s) [5], ν is the kinematic viscosity of electrolyte (0.01 cm^2/s) [6], $c_{0,H+}$ is the bulk concentration of hydronium ions (0.1 M), and ω is the rotating speed of the RDE (unit: rad/s).

Simulation procedure:

The simulation was to solve the governing equations in a 1-dimensional domain from the surface of cathode to the bulk electrolyte during HER in strongly acidic media. The domain for simulation was divided into two regions. The first region was between the surface of cathode and outer Helmholtz plane (OHP), which is called Stern layer. The second region was between OHP and bulk electrolyte, which contained diffuse layer and diffusion layer. Boundary conditions at the surface of cathode, OHP and the bulk-electrolyte side were used to solve the equations (scheme S1).

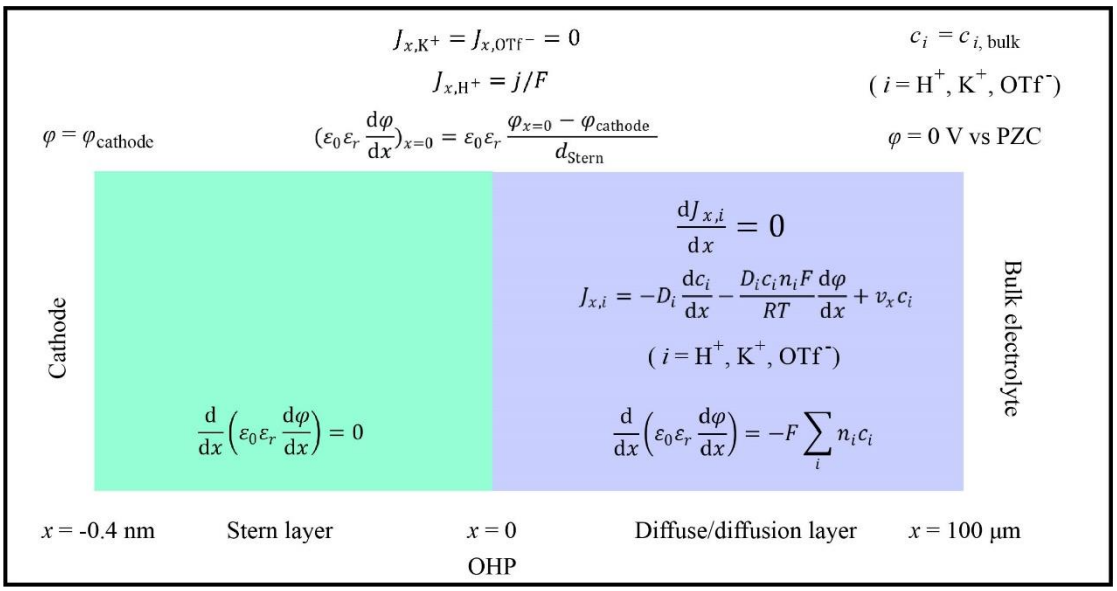

Scheme S1. Governing equations and boundary conditions used for the 1-dimensional simulation. From left to right: the cathode, the Stern layer, the diffuse/diffusion layer, and the bulk electrolyte region. OHP is used as origin (x=0).

The transport of three solvated ionic species (K^+, H^+ and OTf^-) and the corresponding charge transfer were considered in the simulation. The Poisson-Nernst-Planck equations at steady state[7] are solved in the region between OHP and bulk electrolyte. These equations include the diffusion, migration and convection terms of each species:

$$\frac{dJ_{x,i}}{dx} = 0 \qquad \text{(S5)}$$

$$J_{x,i} = -D_i \frac{\mathrm{d}c_i}{\mathrm{d}x} - \frac{D_i c_i n_i F}{RT} \frac{\mathrm{d}\varphi}{\mathrm{d}x} + v_x c_i \quad \text{(S6)}$$

where c_i is the concentration of species i (with i = K^+, H^+ and OTf^-), D_i is the diffusion coefficient of species i, n_i is the charge of species i, R is the ideal gas constant, T is the temperature, F is the Faradaic constant, φ is the potential and v_x is the velocity of solution in *x*-direction. For a rotating disk electrode, the velocity in axial direction at different *x*-locations can be estimated as:[8]

$$v_x = -0.51 x^2 \sqrt{\frac{\omega^3}{\nu}} \quad \text{(S7)}$$

where ω is the rotation speed (unit: rad/s) of the disk electrode, ν is the kinematic viscosity of water.

The Poisson equation is used to calculate the potential change, given by:

$$\frac{\mathrm{d}}{\mathrm{d}x}\left(\varepsilon_0 \varepsilon_r \frac{\mathrm{d}\varphi}{\mathrm{d}x}\right) = -F \sum_i n_i c_i \quad \text{(S8)}$$

where ε_0 is the permittivity of vacuum and ε_r is the relative permittivity of water.

The thickness of Stern layer (d_{Stern}) was assumed to be 0.4 nm.[9] The thickness of the region between OHP and bulk solution in simulation was assumed to be 100 μm, larger than the thickness of diffusion layer for hydronium ions (δ_{H}) estimated by:[8]

$$\delta_{\mathrm{H}} = 1.61 D_i^{1/3} \omega^{-1/2} \nu^{1/6} \quad \text{(S9)}$$

Since hydronium ion has the largest diffusion coefficient, hydronium ion was used to estimate the thickness of the region for simulation. δ_{H} equals 52 μm as the rotating speed was 400 rpm, guaranteeing the region with concentration gradient was included in the domain for simulation.

The boundary conditions for the domain between OHP and bulk electrolyte consist of: At the right side (x = 100 μm), the concentration of each species equals to the bulk concentration of this species, and the potential equals to 0 V vs PZC. At the left side (x = 0), the flux of each species is given as:

$$J_{x,\mathrm{K^+}} = J_{x,\mathrm{OTf^-}} = 0 \quad \text{(S10)}$$

$$J_{x,\mathrm{H^+}} = j/F \quad \text{(S11)}$$

where j is the HER current density and we assumed hydronium ions were the only proton source for HER in strongly acidic media. We assumed the HER current density showed proportional relations with hydronium concentration at OHP and exponential relations with the potential of cathode:

$$j = -Ac_{\mathrm{H^+}}\exp(-\frac{\alpha F}{RT}\varphi_{\mathrm{cathode}}) \quad \text{(S12)}$$

where α is the charge transfer coefficient and $\varphi_{\mathrm{cathode}}$ is the potential of cathode. Then, the HER current densities (j_0 and j_1) at two different conditions ($c^0_{\mathrm{H^+}}$, $\varphi^0_{\mathrm{cathode}}$ and $c^1_{\mathrm{H^+}}$, $\varphi^1_{\mathrm{cathode}}$) show the relationship as:

$$j_1 = j_0 \cdot \frac{c^1_{\mathrm{H^+}}}{c^0_{\mathrm{H^+}}} \cdot \exp(-\frac{\alpha F}{RT}\left(\varphi^1_{\mathrm{cathode}} - \varphi^0_{\mathrm{cathode}}\right)) \quad \text{(S13)}$$

The experimental HER current density on a flat Au electrode at -0.4 V vs SHE in an acidic medium with pH = 1 was -1 mA/cm^2.[10] The PZC of Au in an acidic medium with pH = 1 and containing weakly adsorbed anions (such as SO_4^{2-} and ClO_4^-) was 0.2 V vs SHE.[11] We assumed the PZC of Au in HOTf-KOTf solution with pH = 1 was also 0.2 V vs SHE. Therefore, we assigned $\varphi^0_{\mathrm{cathode}}$ = -0.6 V vs PZC, $c^0_{\mathrm{H^+}}$ = 0.1 M and j_0 = -1 mA/cm^2 in equation S13. We assumed α = 0.5. Then, the HER current density at a certain condition can be estimated as:

$$j = -1\mathrm{mA/cm^2} \cdot \frac{c_{\mathrm{H^+}}}{0.1\ \mathrm{M}} \cdot \exp(-\frac{0.5F}{RT}(\varphi_{\mathrm{cathode}} + 0.6\ \mathrm{V})) \quad \text{(S14)}$$

To confirm that the accuracy of the above assignment did not affect the trends of simulated result, we also did the simulation with the $\varphi^0_{\mathrm{cathode}}$ value in equation S13 as -0.5 V and -0.7 V vs PZC. As shown in fig. S18, as the value of $\varphi^0_{\mathrm{cathode}}$ changed, the current density-potential curves in 0.1 M HOTf or 0.1 M HOTf + 0.4 M KOTf just shifted laterally and the shape of the curves did not change.

In Stern layer, the Poisson equation is given by:

$$\frac{\mathrm{d}}{\mathrm{d}x}\left(\varepsilon_0\varepsilon_r\frac{\mathrm{d}\varphi}{\mathrm{d}x}\right)=0 \quad \text{(S15)}$$

The left boundary condition for equation S15 in Stern layer was:

$$\varphi_{x=-0.4\ \mathrm{nm}}=\varphi_{\mathrm{cathode}} \quad \text{(S16)}$$

Neumann boundary condition was used for equation S8 at OHP (x = 0), namely:

$$(\varepsilon_0\varepsilon_r\frac{\mathrm{d}\varphi}{\mathrm{d}x})_{x=0}=\varepsilon_0\varepsilon_r\frac{\varphi_{x=0}-\varphi_{\mathrm{cathode}}}{d_{\mathrm{Stern}}} \quad \text{(S17)}$$

Table S1 summarizes the values of the various parameters in the model.

Table S1. List of values used for the parameters in the model.

Symbol	Name	Value	Reference
$D_{\mathrm{H^+}}$	Diffusion coefficient of hydronium ion	$9.311\times10^{-9}\ \mathrm{m^2/s}$	5
$D_{\mathrm{K^+}}$	Diffusion coefficient of K^+ ion	$1.957\times10^{-9}\ \mathrm{m^2/s}$	9
$D_{\mathrm{OTf^-}}$	Diffusion coefficient of OTf^- ion	$0.863\times10^{-9}\ \mathrm{m^2/s}$	12
ε_0	Permittivity of vacuum	$8.85\times10^{-12}\ \mathrm{F/m}$	
ε_r	Relative permittivity of water	80.1	9
ν	Kinematic viscosity of water	$1\times10^{-6}\ \mathrm{m^2/s}$	6
T	Temperature	293 K	
R	Ideal gas constant	8.314 J/mol/K	

Numerical details:

A mesh independence study was conducted, resulting in the choice of a uniformly distributed mesh with mesh element size of 0.66×10^{-9} m. A smaller mesh size results in mesh elements smaller than the size of the individual ions. A further decrease in the mesh size resulted in a change in current density, electrolyte potential and concentrations of H^+ and OTf^- of less than 3%. The coupled equations were solved with

a commercial solver (COMSOL 5.5) utilizing a MUMPS solver with a non-linear automatic Newton method. The calculation was done for $\varphi_{\mathrm{cathode}}$ varying between -0.5 V to -1.2 V vs PZC. The solution was converged when a relative tolerance of 0.001 was reached. Further increasing the relative tolerance resulted in a difference in the results of less than 1%. Typically, 10 to 20 iterations were needed for convergence.

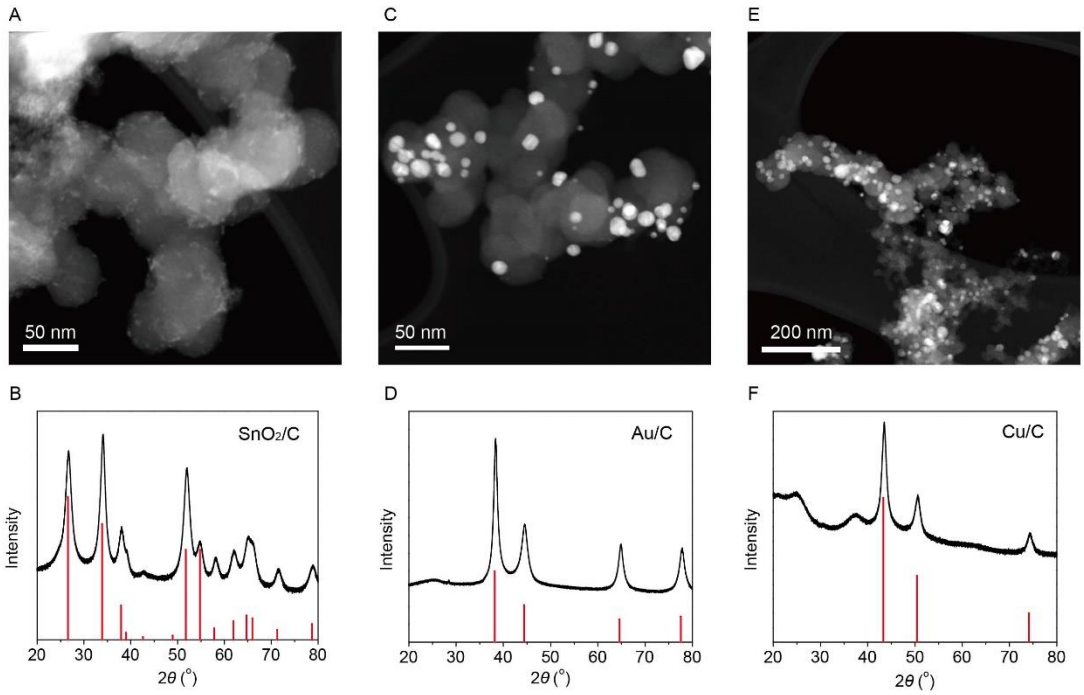

Fig. S1. Characterization of catalysts. (A, C, E) HAADF-STEM images and (B, D, F) PXRD patterns of (A, B) SnO_2/C, (C, D) Au/C and (E, F) Cu/C. The red vertical lines in (B), (D) and (F) are standard diffraction peaks of tetragonal SnO_2 (JCPDS no. 05-0467), face-center-cubic Au (JCPDS no. 04-0784) and face-center-cubic Cu (JCPDS no. 04-0836), respectively.

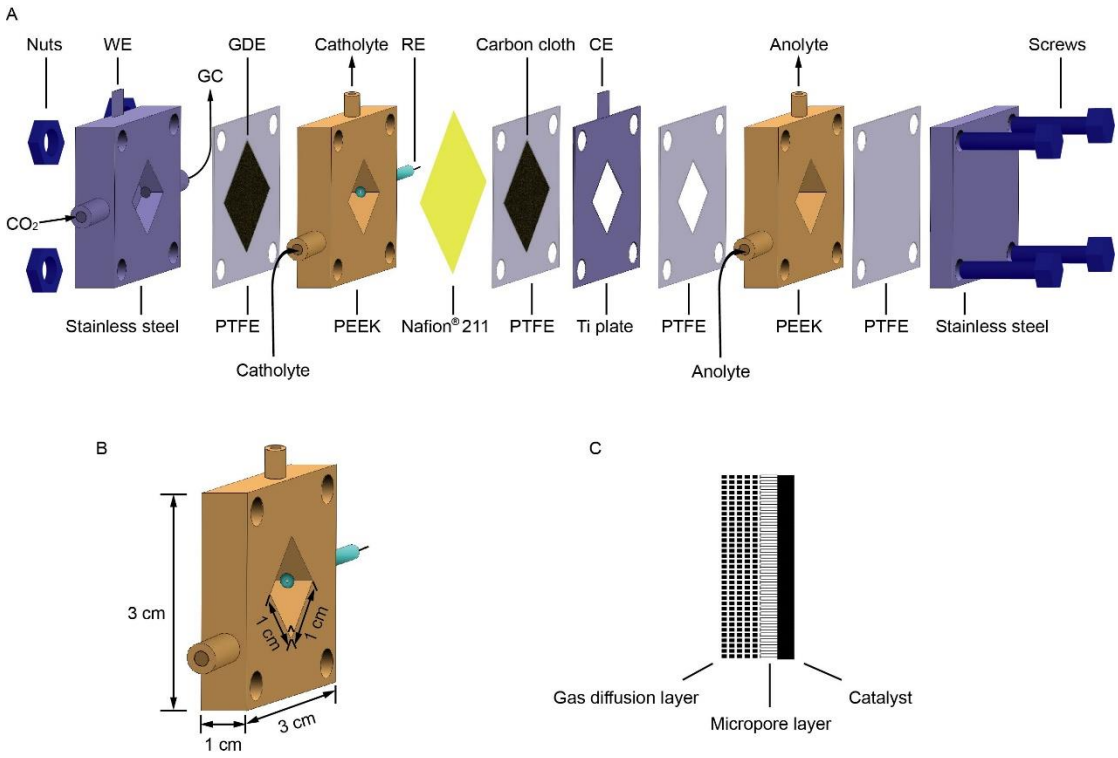

Fig. S2. Scheme of the three-electrode flow cell. (A) Structure of the whole assembly. The material for each part is indicated. WE: working electrode; RE: reference electrode; CE: counter electrode; PTFE: polytetrafluoroethylene; PEEK: polyether ether ketone. (B) Dimensions of the chamber of electrolyte solutions. (C) Scheme of the working electrode. The catalyst was sprayed onto the micropore layer of GDE (CeTech, W1S1009).

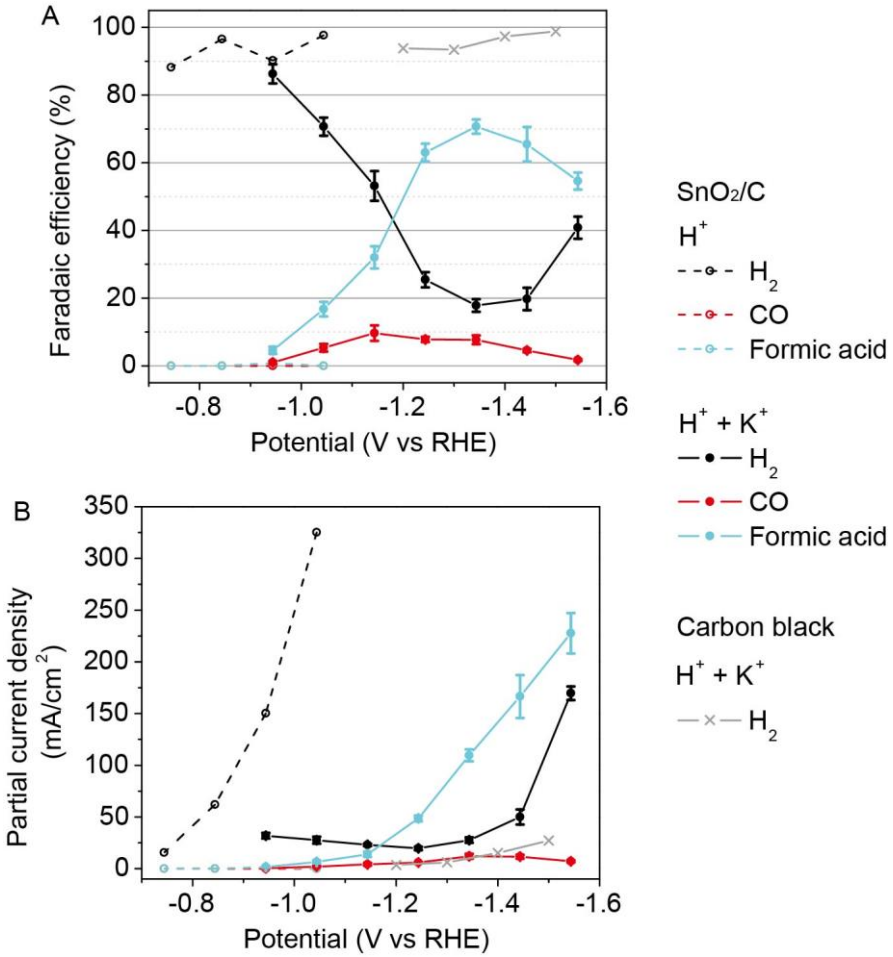

Fig. S3. Comparison of CO_2 reduction in acidic medium with and without K^+ ions. (A) Faradaic efficiency and (B) partial current density of H_2 (black), CO (red) and formic acid (light blue). The catalyst was SnO_2/C. The electrolyte was 0.1 M HOTf (dashed lines) or 0.1 M HOTf + 0.4 M KOTf (solid lines). Faradaic efficiency and partial current density of H_2 of Vulcan XC-72R in 0.1 M HOTf + 0.4 M KOTf was also shown as grey plots.

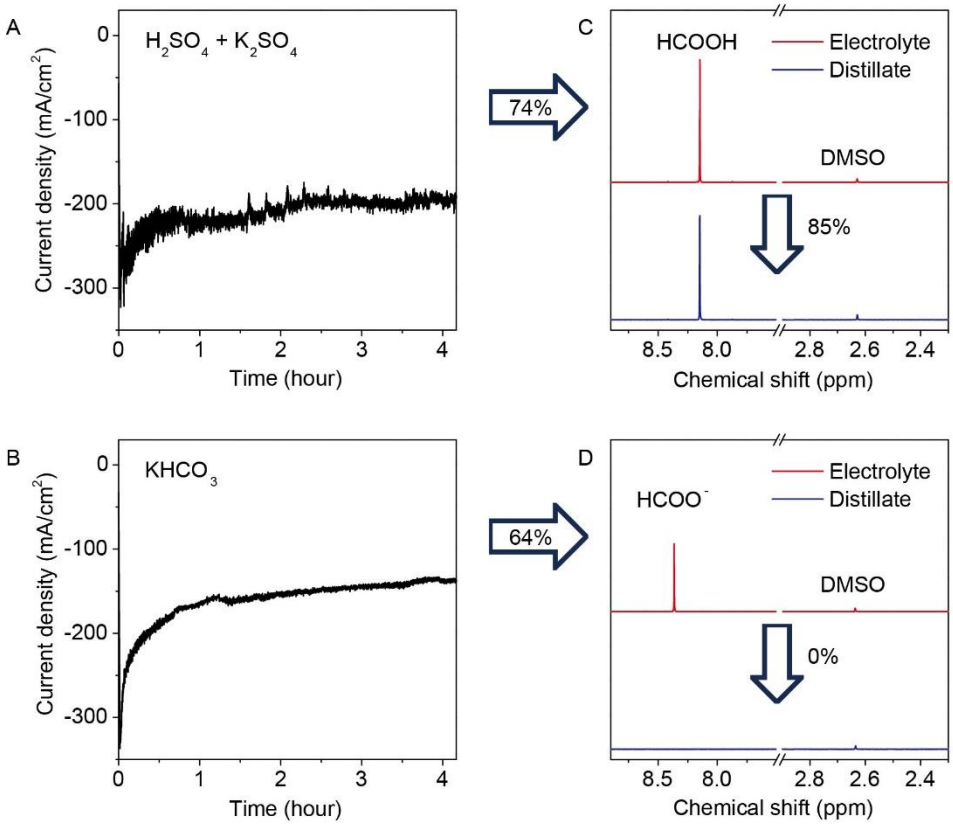

Fig. S4. Analysis and separation of solution-phase product of CO_2 reduction in acidic (0.1 M H_2SO_4 + 0.4 M K_2SO_4) and near neutral (0.8 M $KHCO_3$) media with SnO_2/C catalyst. (A, B) Chronoamperometry curves of SnO_2/C at -1.5 V vs SHE. (C, D) ^{1}H-NMR spectra of electrolyte solution after electrolysis (red) and distillate of electrolyte solution (blue). DMSO was the internal standard. The Faradaic efficiency of formic acid and formate was 74% and 64%, respectively, and the recovery rates of distillation for formic acid and formate are 85% and 0%, respectively. The concentrations of formic acid in the electrolyte solution and the distillate were 1.21 M and 1.03 M, respectively.

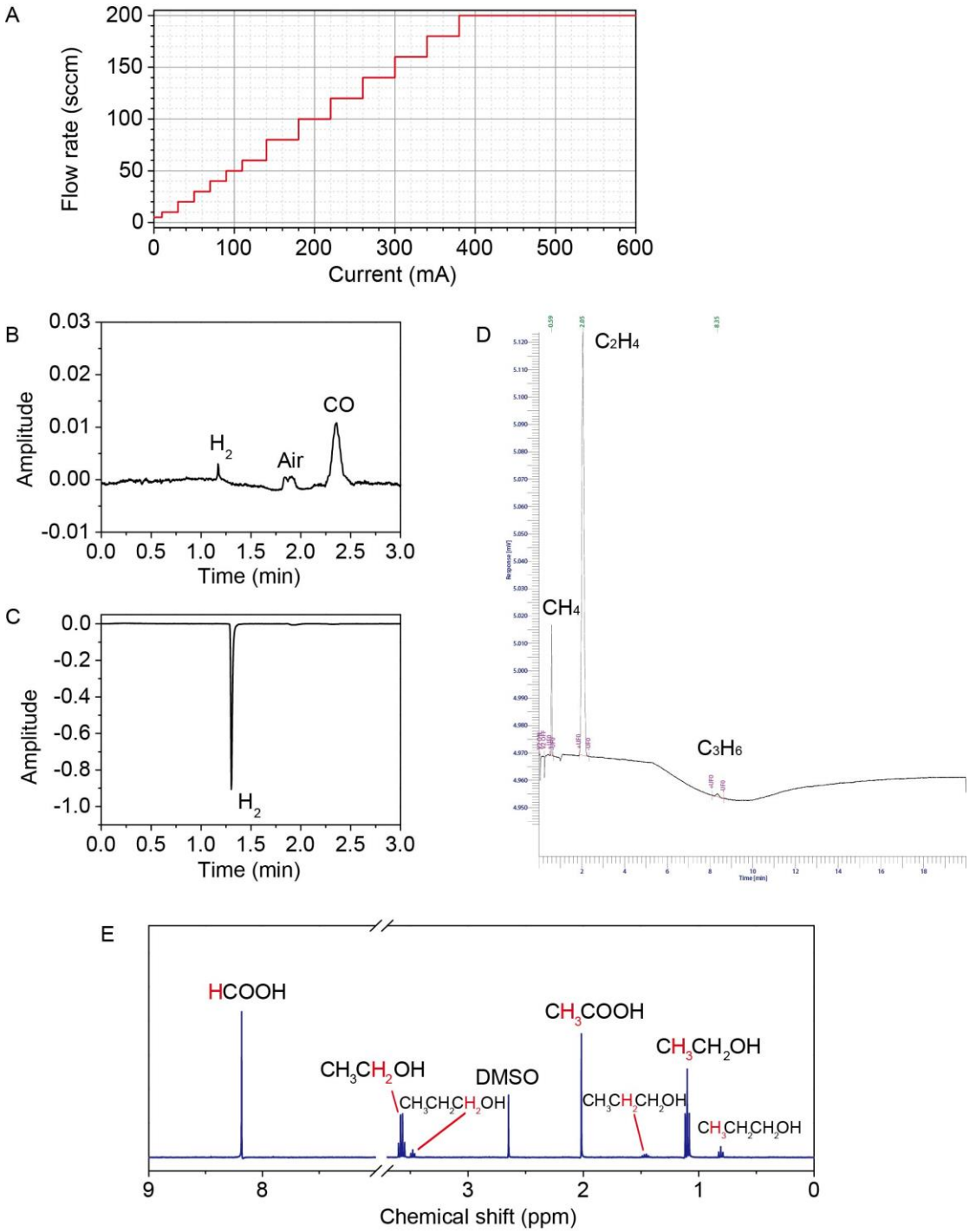

Fig. S5. Products of CO_2 reduction on Cu/C. (A) Tuning the flow rate of CO_2 according to the current of electrolysis. (B) GC-TCD curve with He as the carrier gas. (C) GC-TCD curve with Ar as the carrier gas. (D) GC-FID curve. (E) ^{1}H-NMR spectrum of catholyte solution after electrolysis. For ethanol and 1-propanol, the peaks corresponding to methyl group were used for quantification. Electrolyte: 0.1 M H_2SO_4 + 0.4 M K_2SO_4. Chronoamperometry test at -1.41 V vs RHE for 1800 s.

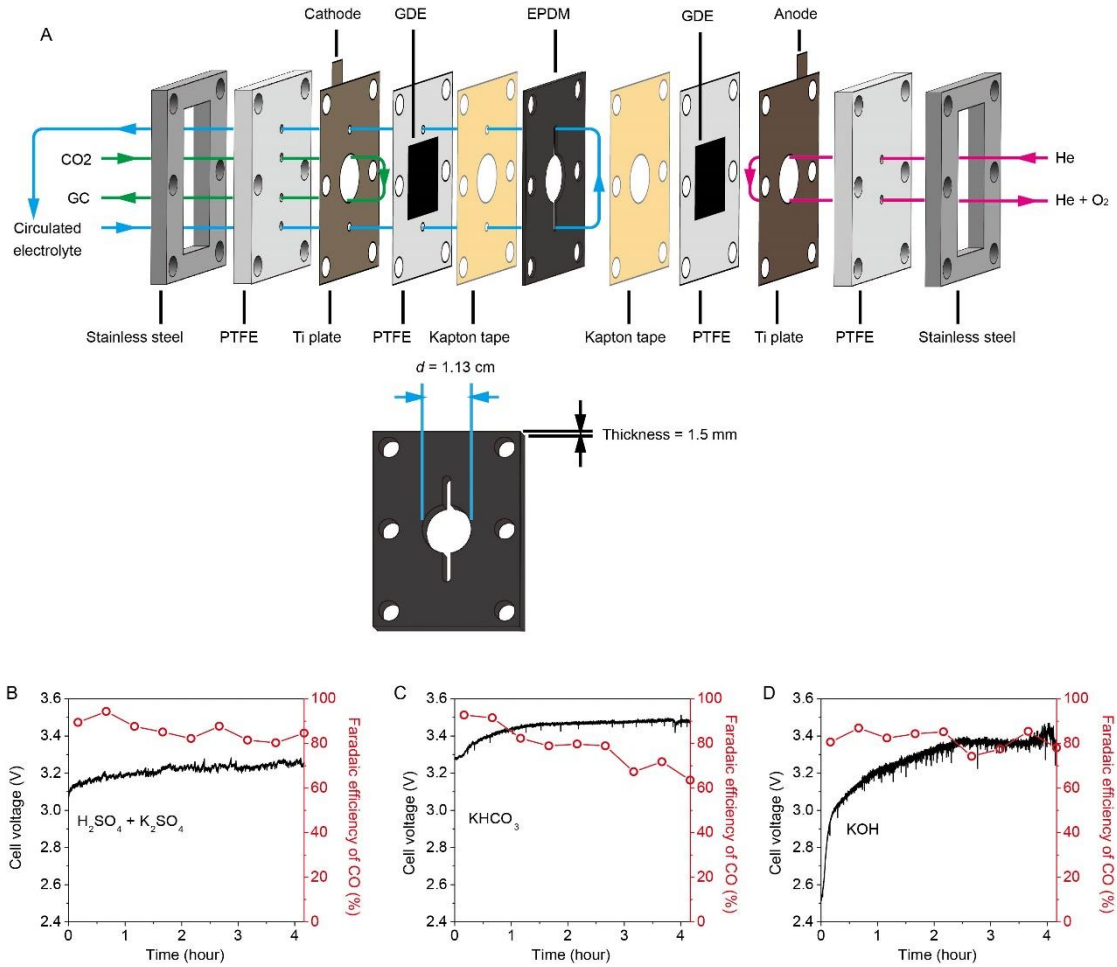

Fig. S6. Electrolysis with two-electrode flow cell. (A) Scheme of the two-electrode flow cell: (top) structure of the whole assembly and (bottom) dimensions of the chamber for the electrolyte solutions. CO_2 electroreduction on Au/C in the two-electrode cell with (B) 0.1 M H_2SO_4 + 0.4 M K_2SO_4, (C) 0.8 M $KHCO_3$, and (D) 0.8 M KOH as the electrolyte solutions. Black curves: cell voltage; red curves: Faradaic efficiency of CO.

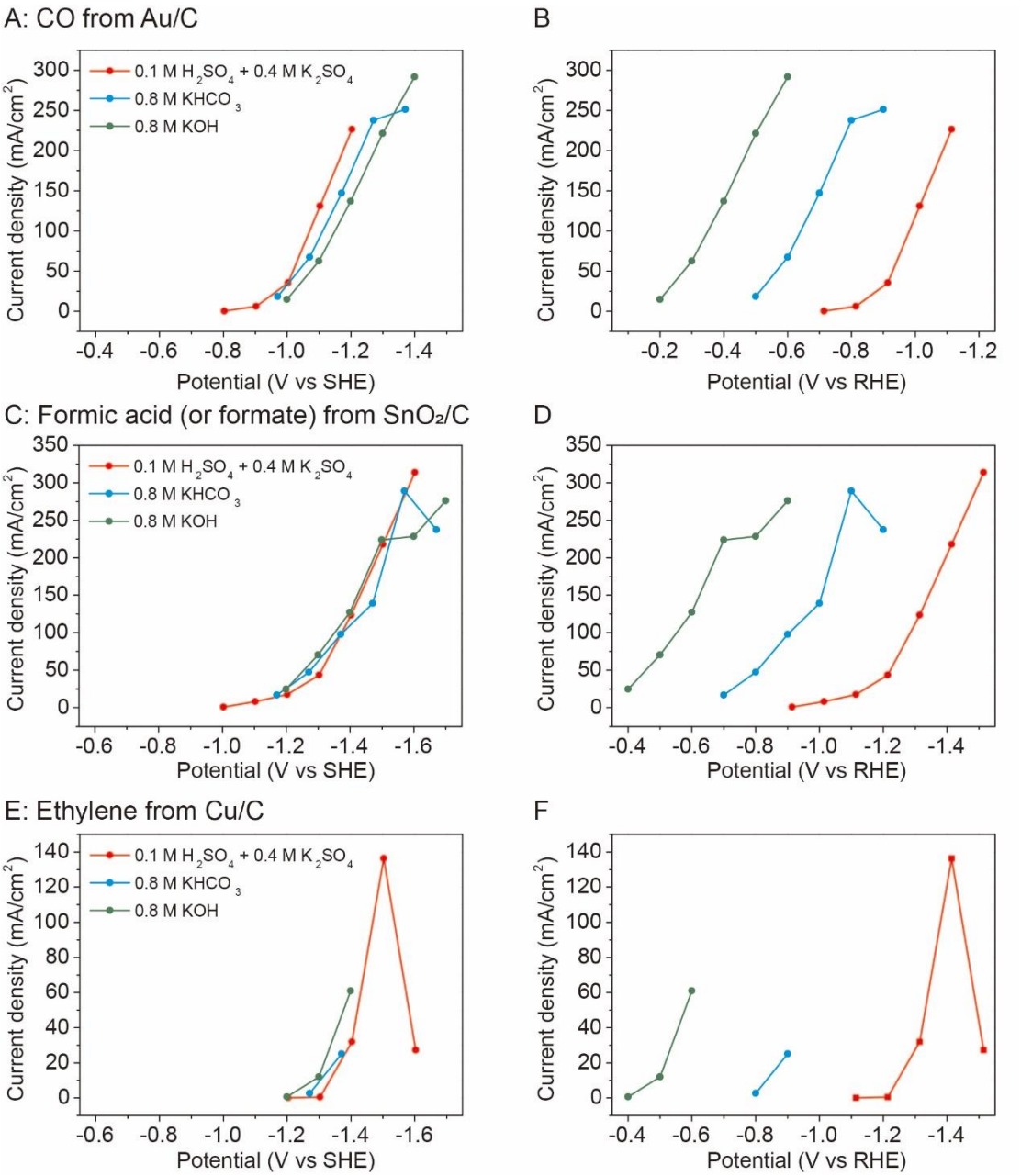

Fig. S7. Plots of partial current density of CO_2 reduction on potential vs SHE and RHE. (A, B) CO formation from Au/C catalyst. (C, D) Formic acid or formate formation from SnO_2/C catalyst. (E, F) Ethylene formation from Cu/C catalyst. (A, C, E) Plots based on SHE. (B, D, F) Plots based on RHE. Electrolyte: (red) 0.1 M H_2SO_4 + 0.4 M K_2SO_4; (blue) 0.8 M $KHCO_3$; (green) 0.8 M KOH.

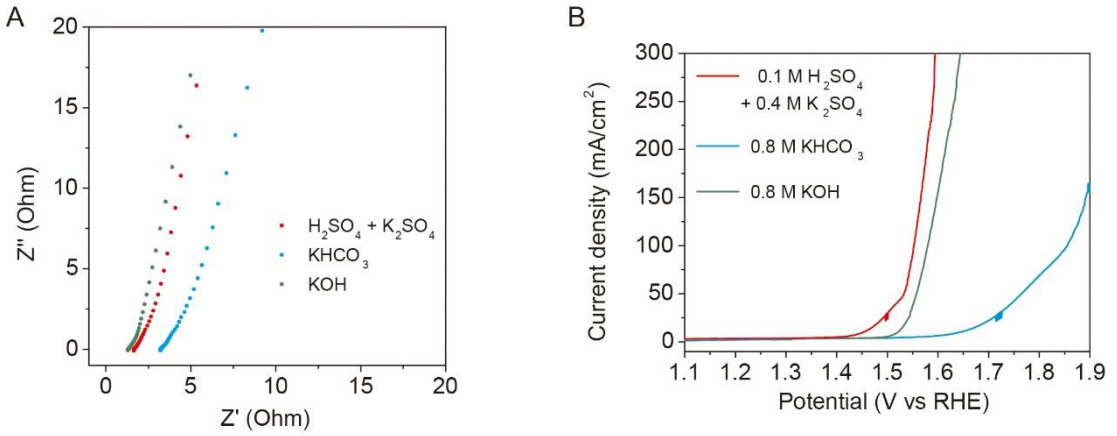

Fig. S8. Resistance and OER overpotential in different media. (A) Nyquest plots at open circuit potential. The real part of high-frequency-limiting impedance is regarded as the resistance of electrolyte solution. Thus, the resistances of 0.1 M H_2SO_4 + 0.4 M K_2SO_4, 0.8 M $KHCO_3$, and 0.8 M KOH, were 1.65 Ω, 3.19 Ω and 1.30 Ω, respectively. (B) LSV curves of IrO_2 anode. The sweeping rate was 20 mV/s. Electrolyte solutions: (red) 0.1 M H_2SO_4 + 0.4 M K_2SO_4; (blue) 0.8 M $KHCO_3$; (green) 0.8 M KOH.

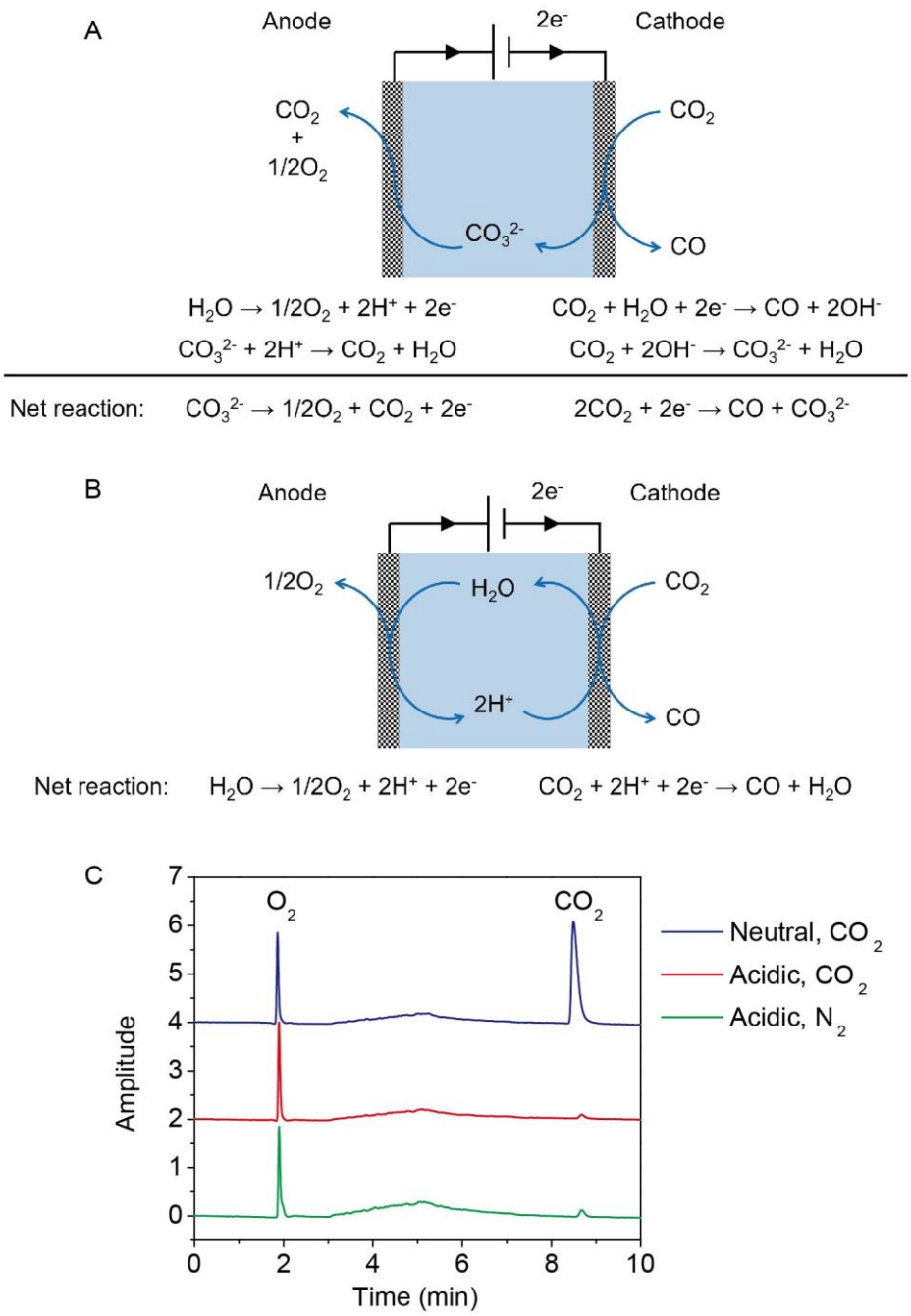

Fig. S9. Carbon efficiency of CO_2 reduction in near neutral and acidic media. Net reactions of CO_2 electrolysis in (A) near neutral and (B) acidic media. In near neutral medium, water molecule is the proton source for cathodic reaction. As one CO_2 molecule is reduced to CO, two OH^- ions are generated, which further react with another CO_2 molecule to form one CO_3^{2-} ion. At anode, OER generates hydronium ions which protonate CO_3^{2-} ions to regenerate CO_2. In acidic medium where the pH is significantly lower than pK_{a1} of H_2CO_3 (3.6), CO_3^{2-} and HCO_3^- ions are not generated from cathode. CO_2 molecules are exclusively converted to reduction products. (C) GC curves of gas generated at the anode compartment. Au/C and IrO_2 were used as catalysts for cathode and anode, respectively. Helium was supplied behind anode. Blue curve: near neutral medium (0.8 M $KHCO_3$) was used and CO_2 was supplied behind the cathode. Red curve:

acidic medium (0.1 M H_2SO_4 + 0.4 M K_2SO_4) was used and CO_2 was supplied behind the cathode. Green curve: acidic medium was used and N_2 was supplied behind the cathode. GC samples were taken after electrolysis at 200 mA/cm^2 for 3 h to ensure the system reached a steady state. The small peaks of CO_2 from acidic medium were due to the oxidation of carbon cloth.

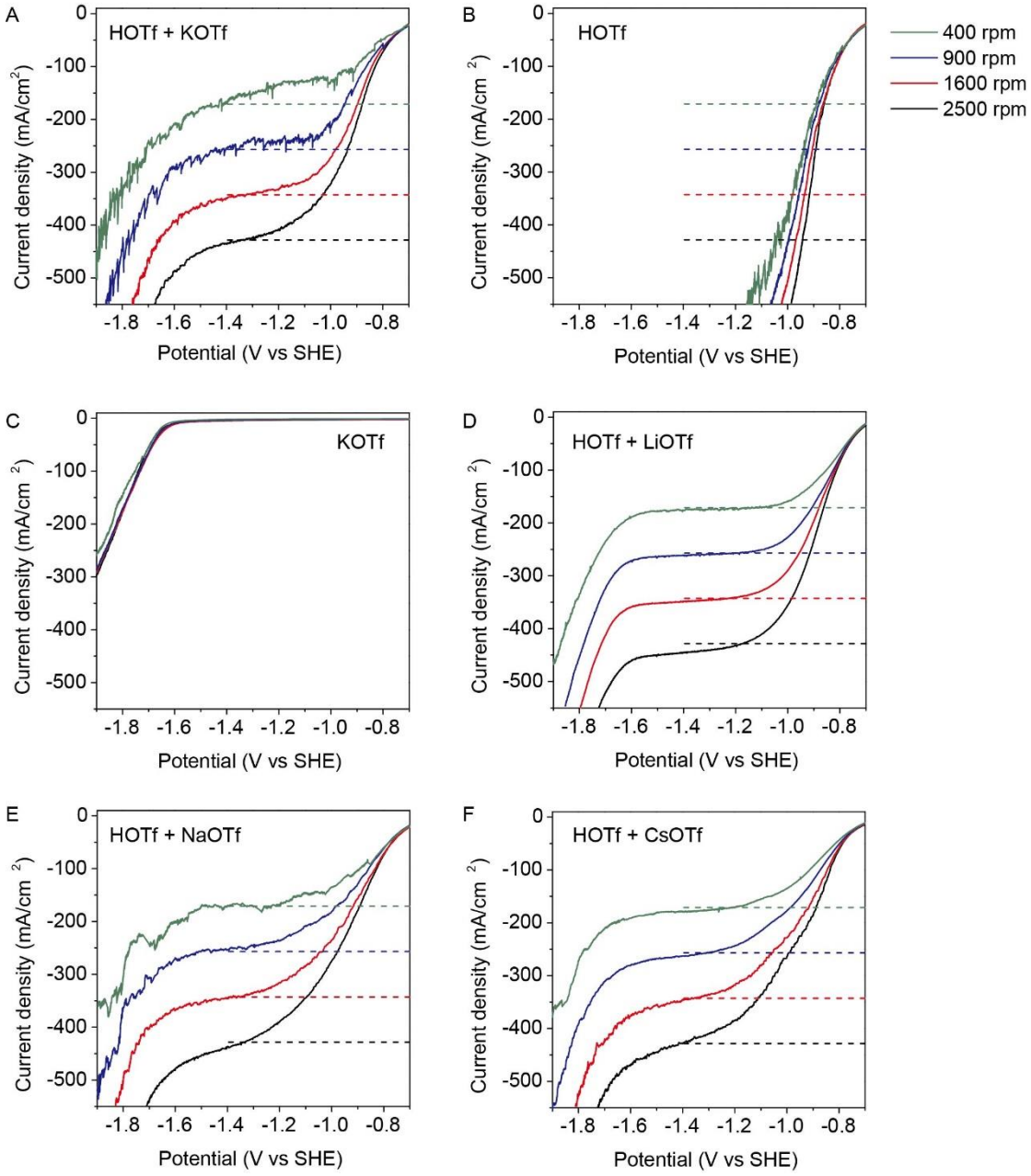

Fig. S10. LSV curves of CO_2 reduction by SnO_2/C on RDE in different electrolyte solutions. (A) 0.1 M HOTf + 0.4 M KOTf. (B) 0.1 M HOTf. (C) 0.4 M KOTf. (D) 0.1 M HOTf + 0.4 M LiOTf. (E) 0.1 M HOTf + 0.4 M NaOTf. (F) 0.1 M HOTf + 0.4 M CsOTf. All electrolyte solutions were saturated with N_2. Rotating speed: 400 rpm (green), 900 rpm (blue), 1600 rpm (red) and 2500 rpm (black). The horizontal dashed lines of each color indicate the limiting diffusion current densities of the reduction of hydronium ions calculated according to Levich equation at the corresponding rotating speeds.

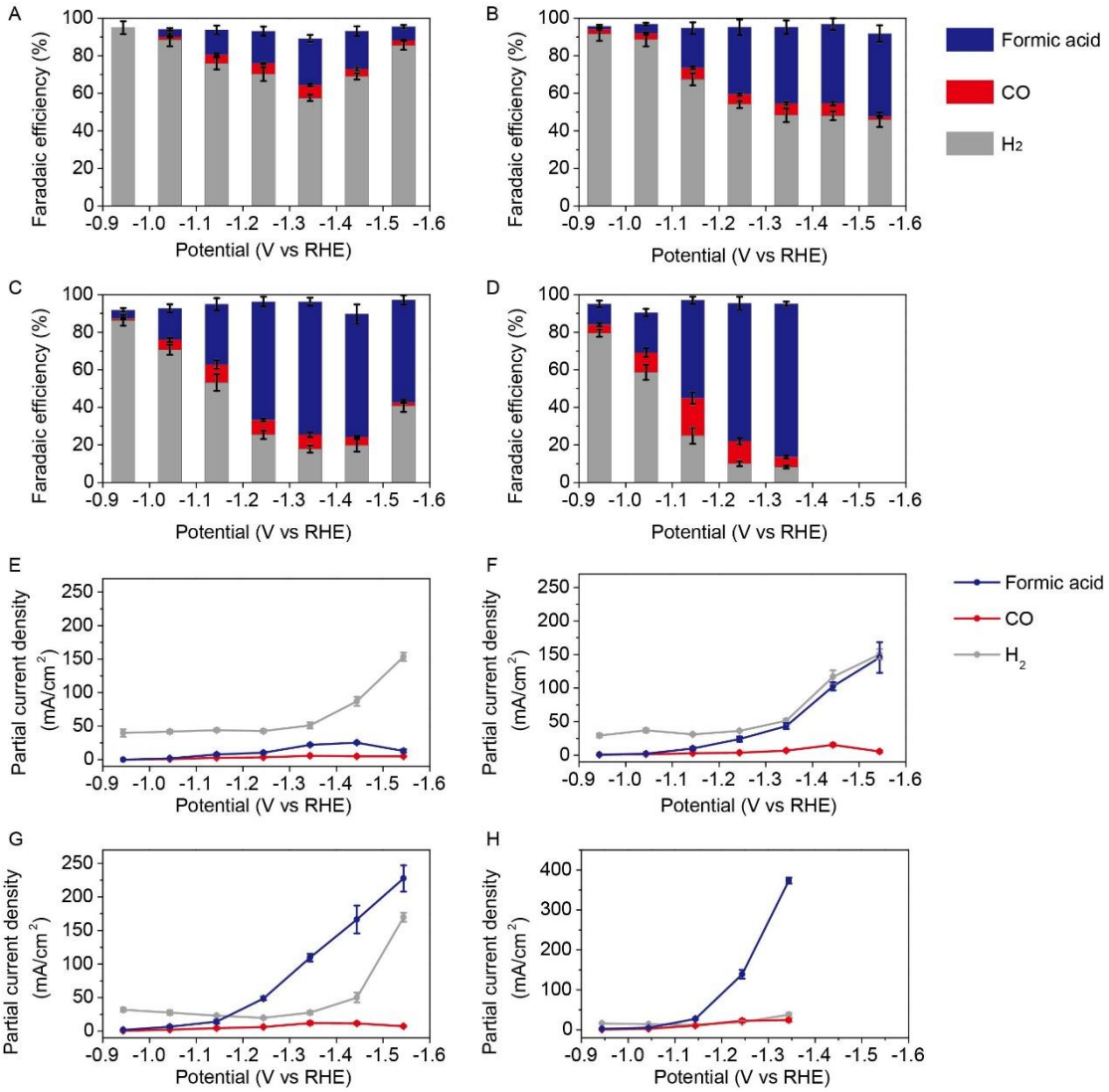

Fig. S11. CO_2 reduction catalyzed by SnO_2/C in acidic medium containing different alkali ions. (A-D) Faradaic efficiency and (E-H) partial current densities of different products. Electrolyte: (A, E) 0.1 M HOTf + 0.4 M LiOTf. (B, F) 0.1 M HOTf + 0.4 M NaOTf. (C, G) 0.1 M HOTf + 0.4 M KOTf. (D, H) 0.1 M HOTf + 0.4 M CsOTf.

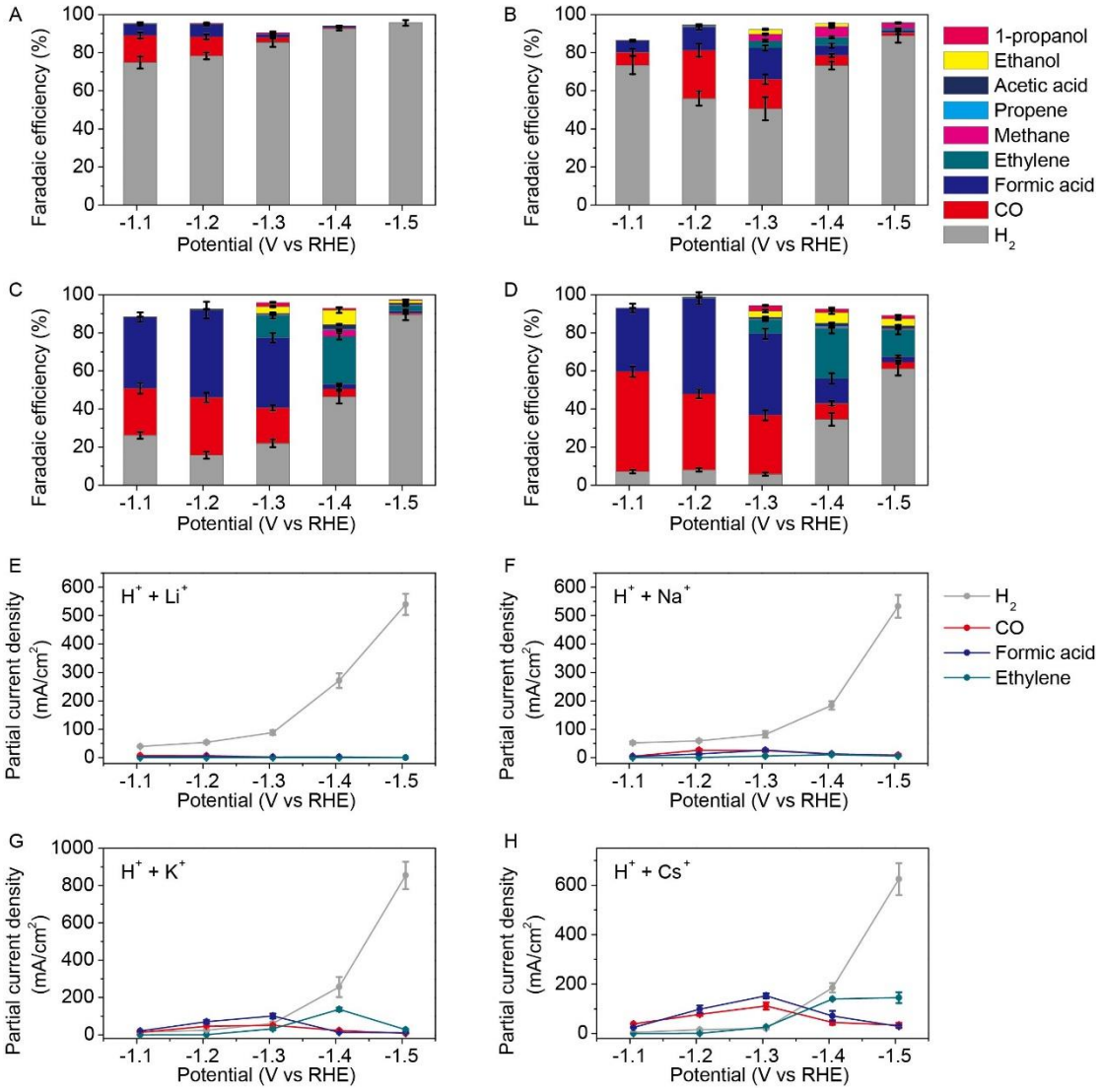

Fig. S12. CO_2 reduction catalyzed by Cu/C in acidic medium containing different alkali ions. (A-D) Faradaic efficiency and (E-H) partial current density of different products. Electrolyte: (A, E) 0.1 M H_2SO_4 + 0.4 M Li_2SO_4. (B, F) 0.1 M H_2SO_4 + 0.4 M Na_2SO_4. (C, G) 0.1 M H_2SO_4 + 0.4 M K_2SO_4. (D, H) 0.1 M H_2SO_4 + 0.4 M Cs_2SO_4.

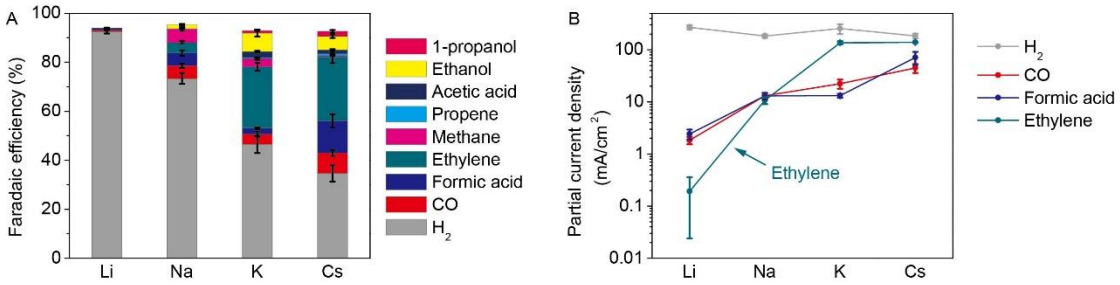

Fig. S13. Cation effects for CO_2 reduction on the Cu/C catalyst. (A) Faradaic efficiency and (B) partial current densities in electrolyte solutions with different alkali ions at -1.41 V vs RHE. The electrolyte was 0.1 M H_2SO_4 + 0.4 M M_2SO_4 (M = Li, Na, K, Cs).

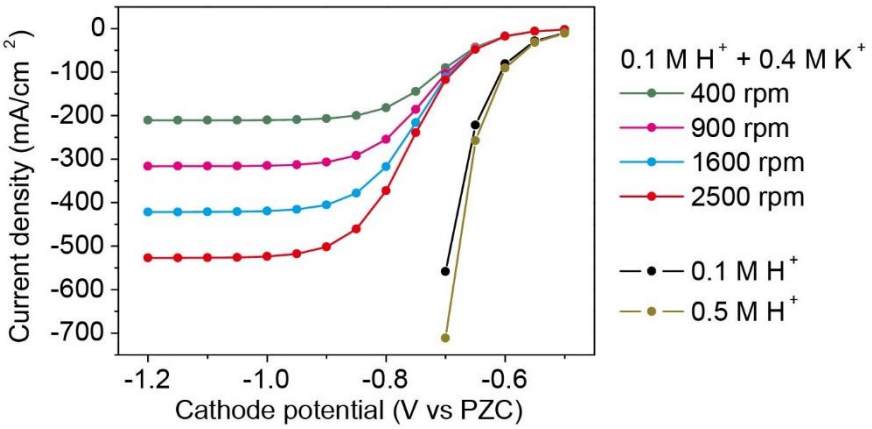

Fig. S14. Simulated HER current density of Au electrode based on PNP model. 0.1 M HOTf + 0.4 M KOTf (green, pink, blue and red curves were simulated with the rotating speed of 400, 900, 1600, and 2500 rpm, respectively), 0.1 M HOTf (black, 1600 rpm) and 0.5 M HOTf (brown, 1600 rpm). It is noteworthy that the plateau current density in 0.1 M HOTf + 0.4 M KOTf is 25% higher than the limiting diffusing current density of hydronium reduction at the corresponding rotating speed based on Levich equation. While in the experimental result in fig. 3A, the plateau current density was about 6% higher than the limiting diffusion current density. This difference was ascribed to that the steric effect of cations was not considered in PNP model. If the steric effect was considered, the repulsion from K^+ ions to H^+ ions near OHP should be stronger, leading to lower concentration of H^+ near cathode and lower HER current density, closer to the HER current density in our experiment observation.

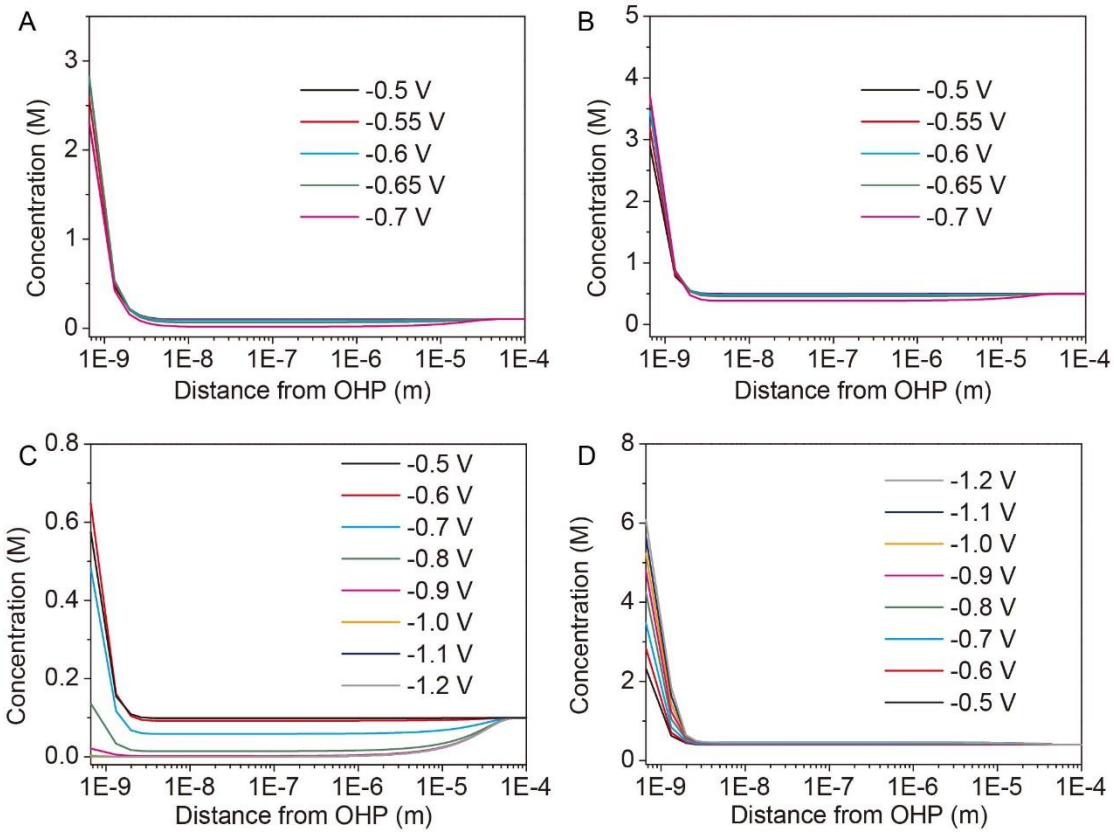

Fig. S15. Concentration profiles of H^+ and K^+ obtained from simulation based on PNP model. (A) Profiles of H^+ in 0.1 M HOTf. (B) Profiles of H^+ in 0.5 M HOTf. (C) Profiles of H^+ in 0.1 M HOTf + 0.4 M KOTf. (D) Profiles of K^+ in 0.1 M HOTf + 0.4 M KOTf. The rotating speed of RDE was 400 rpm. The potentials of cathode are vs PZC.

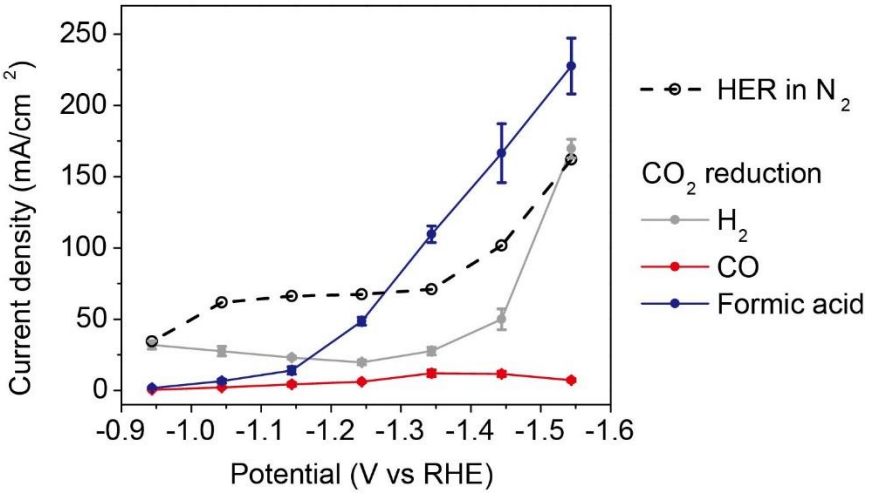

Fig. S16. Comparison of HER in N_2 and CO_2 atmosphere. The catalyst was SnO_2/C and the electrolyte was 0.1 M HOTf + 0.4 M KOTf. The black dashed line shows the current density when N_2 was supplied. The solid lines show the partial current density of H_2 (black), CO (red) and formic acid (blue) when CO_2 was supplied. In N_2 atmosphere, a plateau of current density about 65 mA/cm^2 was observed, corresponding to the diffusion limitation of hydronium ions under this condition. The partial current density of formic acid could be significantly higher than 65 mA/cm^2, indicating water molecules served as the proton source for CO_2 reduction and OH^- ions were generated. The HER current density in CO_2 atmosphere was remarkably lower than in N_2 atmosphere.

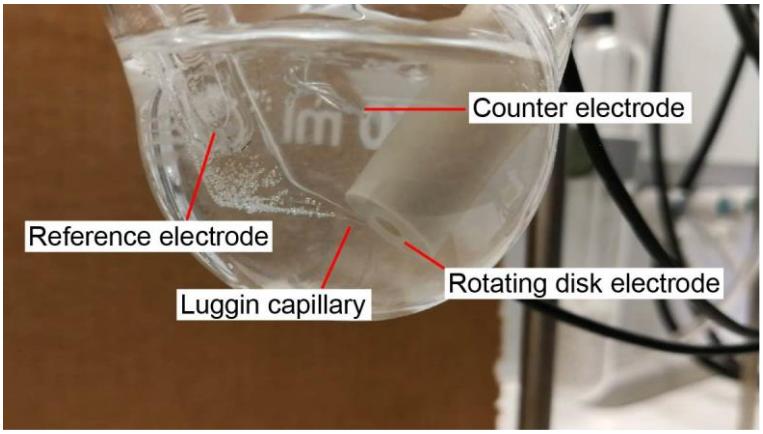

Fig. S17. Set up for RDE experiment. Au RDE in 0.1 M HOTf + 0.4 M KOTf. The current density was -200 mA/cm^2 and the rotating speed was 1600 rpm.

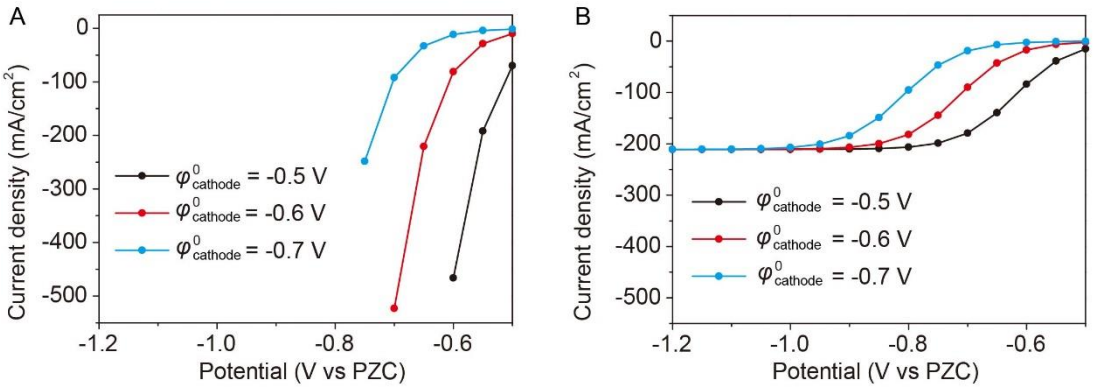

Fig. S18. Simulated HER current density-potential curves with different parameter assignment. (A) In 0.1 M HOTf. (B) In 0.1 M HOTf + 0.4 M KOTf. The $\varphi^0_{\mathrm{cathode}}$ value in equation S13 was set to -0.5 V (black curves), -0.6 V (red curves) and -0.7 V (blue curves), respectively.

References:

1 Gu, J., Héroguel, F., Luterbacher, J. & Hu, X. Densely Packed, Ultra Small SnO Nanoparticles for Enhanced Activity and Selectivity in Electrochemical CO2 Reduction. *Angewandte Chemie International Edition* **57**, 2943-2947, (2018).

2 Wang, Y. *et al.* Ensemble Effect in Bimetallic Electrocatalysts for CO2 Reduction. *Journal of the American Chemical Society* **141**, 16635-16642, (2019).

3 Guo, H. *et al.* Shape-Selective Formation of Monodisperse Copper Nanospheres and Nanocubes via Disproportionation Reaction Route and Their Optical Properties. *The Journal of Physical Chemistry C* **118**, 9801-9808, (2014).

4 Levich, V. G. *Physicochemical Hydrodynamics*. (Prentice-Hall, Englewood Cliffs, 1962).

5 Atkins, P. W. & De Paula, J. *Physical Chemistry, 7th ed.*, 1104 (Oxford University Press, 2002).

6 Grozovski, V., Vesztergom, S., Láng, G. G. & Broekmann, P. Electrochemical Hydrogen Evolution: H+or H2O Reduction? A Rotating Disk Electrode Study. *Journal of The Electrochemical Society* **164**, E3171-E3178, (2017).

7 Newman, J. & Thomas-Alyea, K. E. *Electrochemical Systems*. 3rd edn edn, (John Wiley & Sons, 2004).

8 Bard, A. J. & Faulkner, L. R. *Electrochemical Methods: Fundamentals and Applications*. 2nd Edition edn, (John Wiley & Sons, 2001).

9 Bohra, D., Chaudhry, J. H., Burdyny, T., Pidko, E. A. & Smith, W. A. Modeling the electrical double layer to understand the reaction environment in a CO2 electrocatalytic system. *Energy & Environmental Science* **12**, 3380-3389, (2019).

10 Strmcnik, D. *et al.* Improving the hydrogen oxidation reaction rate by promotion of hydroxyl adsorption. *Nature Chemistry* **5**, 300-306, (2013).

11 Bode, D. D., Andersen, T. N. & Eyring, H. Anion and pH effects on the potentials of zero charge of gold and silver electrodes. *The Journal of Physical Chemistry* **71**, 792-797, (1967).

12 Vanýsek, P. Ionic conductivity and diffusion at infinite dilution, in *Handbook of Chemistry and Physics* (CRC Press, 1992).